

DEVELOPMENTAL NEUROSCIENCE

Asymmetric signaling across the hierarchy of cytoarchitecture within the human connectome

Linden Parkes^{1*}, Jason Z. Kim^{1†}, Jennifer Stiso^{1†}, Monica E. Calkins^{2,3}, Matthew Cieslak^{2,3,4}, Raquel E. Gur^{2,3,5,6}, Ruben C. Gur^{2,3,5,6}, Tyler M. Moore^{2,3}, Mathieu Ouellet⁷, David R. Roalf^{2,3}, Russell T. Shinohara^{4,8}, Daniel H. Wolf^{2,4}, Theodore D. Satterthwaite^{2,3,4}, Dani S. Bassett^{1,2,5,7,9,10}

Cortical variations in cytoarchitecture form a sensory-fugal axis that shapes regional profiles of extrinsic connectivity and is thought to guide signal propagation and integration across the cortical hierarchy. While neuroimaging work has shown that this axis constrains local properties of the human connectome, it remains unclear whether it also shapes the asymmetric signaling that arises from higher-order topology. Here, we used network control theory to examine the amount of energy required to propagate dynamics across the sensory-fugal axis. Our results revealed an asymmetry in this energy, indicating that bottom-up transitions were easier to complete compared to top-down. Supporting analyses demonstrated that asymmetries were underpinned by a connectome topology that is wired to support efficient bottom-up signaling. Lastly, we found that asymmetries correlated with differences in communicability and intrinsic neuronal time scales and lessened throughout youth. Our results show that cortical variation in cytoarchitecture may guide the formation of macroscopic connectome topology.

INTRODUCTION

Multiple lines of evidence suggest that the brain's extrinsic structural connectivity is predicted from its cytoarchitecture (1, 2). This structural model suggests that the degree to which two regions share similar cytoarchitectural features predicts the distribution of their laminar projections. Critically, interregional similarity in cytoarchitecture varies gradually across the cortex, creating a sensory-fugal (S-F) axis (3, 4) that predicts regions' profiles of extrinsic connectivity to the rest of the brain. This gradient positions contiguous visual and sensorimotor cortex at one end and distributed heteromodal association and paralimbic cortices at the other and is correlated with other macroscopic gradients of brain structure and function (5). Together, these multimodal gradients form a hierarchy of brain organization that is thought to govern extrinsic connectivity (1) and support the efficient propagation and integration of signals across the cortex (6–8). However, the extent to which cytoarchitecture's governance over connectivity manifests in the topology of the macroscopic structural connectome remains a key open question. Here, we examine whether the S-F axis constrains signal propagation across macroscopic connectome topology.

¹Department of Bioengineering, School of Engineering and Applied Science, University of Pennsylvania, Philadelphia, PA 19104, USA. ²Department of Psychiatry, Perelman School of Medicine, University of Pennsylvania, Philadelphia, PA 19104, USA. ³Lifespan Brain Institute, University of Pennsylvania and Children's Hospital of Philadelphia, Philadelphia, PA 19104, USA. ⁴Center for Biomedical Image Computing and Analytics, Perelman School of Medicine, University of Pennsylvania, Philadelphia, PA 19104, USA. ⁵Department of Neurology, Perelman School of Medicine, Philadelphia, PA 19104, USA. ⁶Department of Radiology, Perelman School of Medicine, Philadelphia, PA 19104, USA. ⁷Department of Electrical and Systems Engineering, School of Engineering and Applied Science, University of Pennsylvania, Philadelphia, PA 19104, USA. ⁸Penn Statistics in Imaging and Visualization Center, Department of Biostatistics, Epidemiology, and Informatics, Perelman School of Medicine, University of Pennsylvania, Philadelphia, PA 19104, USA. ⁹Department of Physics and Astronomy, College of Arts and Sciences, University of Pennsylvania, Philadelphia, PA 19104, USA. ¹⁰Santa Fe Institute, Santa Fe, NM 87501, USA.

*Corresponding author. Email: lindenmp@seas.upenn.edu

†These authors contributed equally to this work.

Convergent evidence spanning the past three decades supports the premise that neuronal signaling is shaped and constrained by a globally ordered cortical hierarchy (6, 7, 9, 10). External stimuli arrive at functionally specialized sensory cortices before propagating up modality-specific hierarchies to then apex at association and paralimbic regions responsible for functional integration. This convergent bottom-up signal propagation is complemented by far-reaching modulatory top-down signals (11–14) that operate on longer time scales (15) and that bind incoming sensory signals together to update predictive inferences about our environment and to complete goal-directed action (16, 17). Critically, these cooperative patterns of bottom-up and top-down signaling, and the asymmetries between them (13), may be underpinned by graded variations in cortical cytoarchitecture (1, 18, 19). Specifically, regions' cytoarchitecture robustly predicts their extrinsic connectivity profiles (20), including the strength (21), distance (21), and layer origination and termination (21, 22) of feedforward and feedback projections (13). Furthermore, interregional similarity in cytoarchitecture follows a clear S-F axis (3, 4), suggesting that where a region is situated along the cortical hierarchy characterizes its bottom-up and top-down connectivity with the rest of the brain and thus explains its capacity to support signal propagation across the hierarchy. Consistent with this notion, regional variation in the depth-wise T1-weighted/T2-weighted ratio—an in vivo neuroimaging measurement that correlates with the S-F axis of cytoarchitecture (3, 23)—couples with the regions' intrinsic time scales of neuronal activity (24), demonstrating that cytoarchitecture tracks the progressive lengthening of neuronal oscillations associated with hierarchical information integration (15). In addition, the S-F axis also correlates with regional weighted degree from diffusion-weighted structural networks (25), demonstrating that cytoarchitecture tracks local properties of macroscopic connectome topology.

Regional variations to cytoarchitecture are, in part, rooted in neurodevelopment (1, 18, 20, 26–30). During prenatal development, differences in the developmental timing of neurogenesis

Copyright © 2022
The Authors, some
rights reserved;
exclusive licensee
American Association
for the Advancement
of Science. No claim to
original U.S. Government
Works. Distributed
under a Creative
Commons Attribution
NonCommercial
License 4.0 (CC BY-NC).

Downloaded from <https://www.science.org> on February 26, 2023

lead to highly eulaminate regions—such as the primary visual cortex—developing more slowly than agranular regions (31), suggesting that prenatal development lays the foundation for the S-F axis. Once laid, the S-F axis scaffolds the formation of extrinsic feed-forward and feedback connections that traverse up and down the hierarchy (1). This connectivity formation also appears to track the S-F axis in a developmentally staged manner, with synaptogenesis peaking earlier in lower-order primary visual areas than in the higher-order frontal cortex (32–34). Furthermore, neuroimaging research shows that macroscopic proxies of the S-F axis (e.g., T1-weighted features), as well as structural connectivity, continue to change throughout postnatal development (5, 35–41), suggesting that the S-F axis continues to shape connectome topology.

As the above literature demonstrates, the processes that govern the patterns of extrinsic connectivity across the cortex are encoded by regional variations in cytoarchitecture, and this regional variation provides a blueprint for the refinement of connectivity throughout development. However, the extent to which the topology of the structural connectome can be leveraged to model bottom-up and top-down signal propagation across the S-F axis remains unknown. The literature reviewed above leads us to four predictions. First, if differences in extrinsic projections encoded by cytoarchitecture are reflected in connectome topology (25), then we should be able to model asymmetries between bottom-up and top-down signal propagation across the S-F axis in humans in vivo. Notably, recent work has shown that the topology of the undirected structural connectome generates spatially varied patterns of signal propagation (42) and asymmetric signaling (43), suggesting that such asymmetry may be assessable using noninvasive neuroimaging. Second, if asymmetric signal propagation is produced specifically by the cytoarchitectonic hierarchy, then asymmetries may not generalize to different definitions of the cortical hierarchy that only partially correlate with the S-F axis, such as those derived from the T1w/T2w ratio (23) and functional connectivity (44). Third, because signals propagating across the S-F axis will traverse through changing temporal receptive windows (24), we expect

asymmetries to correlate with differences in intrinsic neuronal time scales. Fourth, if signal propagation continues to be refined throughout development, then asymmetries should vary systematically as a function of age in youth.

To evaluate evidence for the above reasoning, we turned to the minimum control energy framework from the network control theory (NCT) (45, 46). Using a linear model of dynamics, NCT estimates the amount of input energy—delivered to a set of control nodes (brain regions)—that is required to drive the brain to transition between pairs of activity states. In this context, we consider binary states in which one set of regions is active while the rest of the brain is inactive. Here, we sought to estimate the transition energy associated with trans-hierarchical state transitions. We found that bottom-up state transitions were more efficient (required less energy) compared to top-down transitions. We also observed that the hierarchical distance separating brain states correlated with the size of these energy asymmetries, suggesting that states with different underlying cytoarchitecture display the most pronounced asymmetries. In addition to these primary findings, we examined (i) whether our findings generalized to the T1w/T2w ratio (23) and the principal gradient of functional connectivity (44), (ii) whether our transition energies correlated with between-state differences in intrinsic time scales, (iii) whether brain regions' position along the S-F axis explained their role in facilitating state transitions, and (iv) whether energy asymmetries correlated with age in a developing sample of youths. Our work extends the field's understanding of connectome topology by showing that the neuroanatomical processes that give rise to extrinsic connectivity constrain the directional flow of macroscopic dynamics over the cortex.

RESULTS

Mapping trans-hierarchical state transitions

We characterized the energy required to complete trans-hierarchical state transitions. Here, we set our brain states to actuate patches

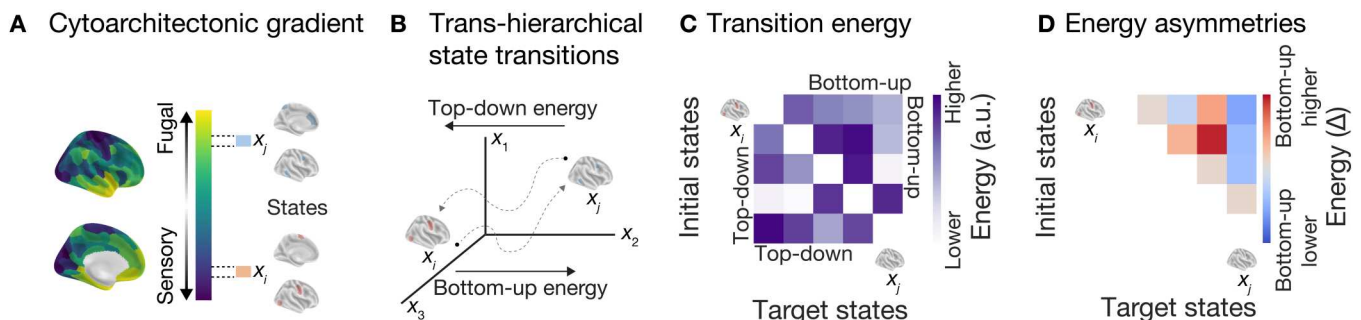


Fig. 1. Estimating trans-hierarchical signal propagation. Using the Schaefer atlas, we sampled 20 nonoverlapping groups of regions ($n = 10$ per state) traversing up the S-F gradient of cytoarchitectonic similarity (4). These groups formed brain states spanning the cortical hierarchy. By definition, regions within each state had relatively similar profiles of cytoarchitecture. Accordingly, pairs of states separated by long hierarchical distances have different underlying cytoarchitecture. (A) An example pair of brain states (x_i, x_j) at different locations along the S-F axis. (B) For a given pair of states (x_i, x_j), we calculated the minimum control energy (E) required to complete the transition from x_i to x_j and from x_j to x_i . (C) Minimum control energy between all pairs of states was assembled into a transition energy matrix, T_E . Owing to the ordered nature of our brain states, transition energies were trivially grouped into bottom-up (transitions moving up the hierarchy; T_E , upper triangle) and top-down (transitions moving down the hierarchy; T_E , lower triangle). a.u., arbitrary units. (D) Given this grouping, we subtracted top-down energy from bottom-up energy to create an energy asymmetry matrix ($T_{E\Delta}$). In the upper triangle of this asymmetry matrix, positive values represented state transitions where bottom-up energy was higher than top-down energy, whereas negative values represented the opposite. Note that, apart from the sign of the Δ value, $T_{E\Delta}$ is symmetric; hence, all analyses of asymmetries focused on the upper triangle of this matrix.

of the cortex with relatively homogeneous profiles of cytoarchitecture. Briefly, we defined the cortical hierarchy as the S-F axis of cytoarchitectonic similarity (fig. S1A) developed in previous work (3, 47) and disseminated as part of the BigBrainWarp toolbox (4) (see Materials and Methods). We selected this S-F axis as it represents the current state-of-the-art proxy of continuously varying profiles of cytoarchitecture in the human brain. Next, we defined brain states by splitting the S-F axis into k equally sized nonoverlapping groups of regions that spanned the gradient (Fig. 1A; see Materials and Methods). Then, using a group-averaged structural connectome, A , taken from the Philadelphia Neurodevelopmental Cohort (PNC) [see Materials and Methods; $N = 793$ (458 females), mean age = 15.66 ± 3.3 years] (48), we modeled the transition energy between all k pairs of brain states, generating a $k \times k$ matrix of energy values, T_E (Fig. 1, B and C). Critically, the hierarchically ordered nature of our brain states meant that bottom-up transition energies were naturally stored in the upper triangle of T_E , while top-down transition energies were stored in the lower triangle. We computed energy asymmetries by subtracting top-down energy from bottom-up energy (Fig. 1D; $T_{E\Delta} = T_E - T_E^T$). In the upper triangle of $T_{E\Delta}$, positive values indicate bottom-up energy being greater than top-down energy, whereas negative values indicate bottom-up energy being lower than top-down energy.

We found that bottom-up energy was significantly lower than top-down energy [Fig. 2A, left; mean energy asymmetry = -0.60 , bootstrapped 95% confidence interval (CI) = $[-0.62, -0.59]$], demonstrating that state transitions moving up the cytoarchitectonic S-F axis required less energy (i.e., were easier to complete; see Materials and Methods) compared to those moving down the same axis (see fig. S2 for first-order statistical features of the bootstrapped connectomes). Furthermore, in support of our hypothesis, we found that the hierarchical distance between brain states was negatively correlated with $T_{E\Delta}$ (Fig. 2B, left; Spearman's $\rho = -0.32$, bootstrapped 95% CI = $[-0.33, -0.31]$). That is, as states' cytoarchitecture became more dissimilar from one another (greater hierarchical distance), energy asymmetries became more negative. Thus, asymmetries between bottom-up and top-down transition energies were largest when brain states had differing cytoarchitecture, with bottom-up transitions becoming progressively easier to complete than top-down. These findings were highly robust to the choice of normalization constant, c , and time horizon, T , in our model (fig. S3; see Materials and Methods). In addition, we found convergent results when we (i) generated a new group-averaged connectome using only individuals who were at least 20 years old ($N = 69$; mean energy asymmetry = -0.55 ; correlation with hierarchical distance, $\rho = -0.29$) and (ii) ran new analyses on a single hemisphere, thereby excluding interhemispheric connections (mean energy asymmetry = -0.64 ; correlation with hierarchical distance, $\rho = -0.30$).

Next, to examine whether the above energy asymmetries depended on topology, we recomputed $T_{E\Delta}$ under two null network models. Specifically, we randomly rewired the underlying group-averaged structural connectome 10,000 times using a spatially embedded permutation model that preserved either the edge distribution or the strength distribution of the network (see Materials and Methods) (49). Then, for every rewired connectome, we reestimated $T_{E\Delta}$ and the correlation with hierarchical distance. We found that both the mean energy asymmetry (Fig. 2A, right) and the hierarchy distance correlation (Fig. 2B, right) were stronger than expected

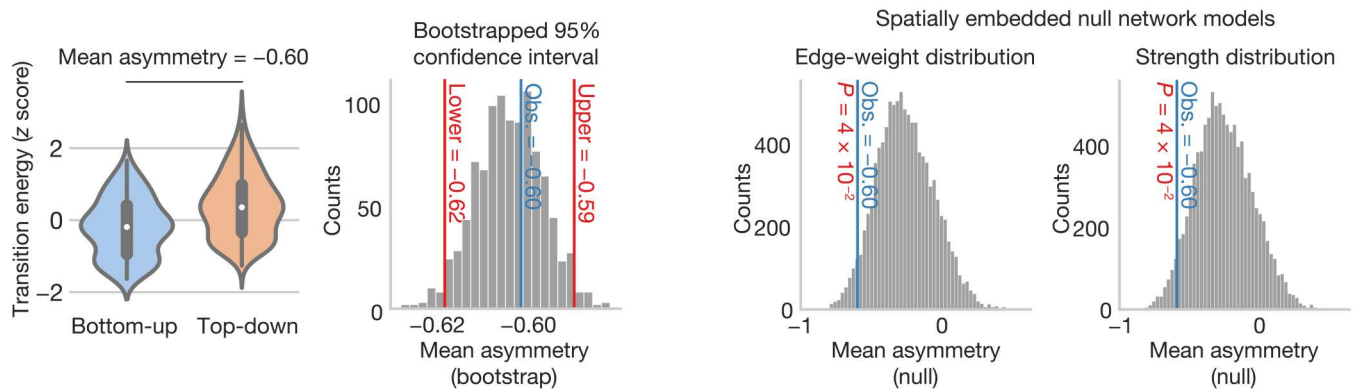
under both null distributions. These results demonstrate that energy asymmetries, as well as the negative correlation with hierarchical distance, were not explained by a combination of the network's spatial embedding and edge (or strength) distribution. In turn, these effects may be explained by variations in cytoarchitectonic profiles.

Having demonstrated that energy asymmetries were not explained by lower-order topology of the human connectome, we next sought to characterize potential higher-order features that may explain these effects. To achieve this goal, we leveraged two metrics of internodal communication that are sensitive to the asymmetric signaling embedded in connectome topology: diffusion efficiency (de) and search information (si) (see Materials and Methods) (43). The metric de quantifies the efficiency of signal propagation from node i to node j under a diffusion model (50). The metric si quantifies the probability that a random walker will arrive at node j by following the shortest path from node i (51); lower si indicates a higher probability of finding the shortest path. We subtracted de_{ji} from de_{ij} and si_{ji} from si_{ij} to create de_{Δ} and si_{Δ} . In addition, to provide deeper intuition, we developed a modified version of path transitivity (pt) (52) that was sensitive to asymmetry (see Materials and Methods). Given the shortest path between a pair of nodes, path transitivity measures the extent to which activity deviates from, but then returns to, the shortest path (Fig. 3A); high pt indicates the presence of paths wherein detours return to the path, whereas low pt indicates the presence of detours that do not return. The standard implementation of pt is symmetric (52). To introduce asymmetry, we examined the cumulative pt (pt_c ; see Materials and Methods) of a given shortest path. Specifically, pt_c was obtained by calculating pt separately for successively longer segments of the shortest path in both directions (Fig. 3B). This approach created a pair of transitivity curves (Fig. 3C)—one for each direction—that both culminated in the same full-path pt value (see fig. S4 for plots of these curves for a subset of the longest paths in A). Subtracting these curves and summing the differences yielded a difference score, $pt_{c\Delta}$, that encoded the extent to which returning detours were encountered sooner or later when traveling one direction along the path compared to the other.

We quantified each of these asymmetric communicability metrics (de_{Δ} , si_{Δ} , and $pt_{c\Delta}$) between all pair of nodes in A and then averaged over the values that connected our brain states (see fig. S5 for correlations between the S-F axis and node-averaged communicability metrics). We found that $T_{E\Delta}$ correlated negatively with de_{Δ} (Fig. 3D) and positively with si_{Δ} (Fig. 3E) and $pt_{c\Delta}$ (Fig. 3F). These results indicate that state transitions with lower bottom-up energy (relative to top-down) are also associated with (i) higher bottom-up diffusion efficiency, (ii) lower bottom-up search information, and (iii) lower bottom-up cumulative path transitivity. In turn, these results suggest that bottom-up signaling is more efficient than top-down (higher bottom-up de) in part because it is more likely to find the shortest paths (lower bottom-up si). In addition, returning detours are encountered sooner for top-down signaling (lower bottom-up pt_c /higher top-down pt_c), which indicates that the early occurrence of these detours may inhibit top-down signaling.

Lastly, to test whether our results were specific to the S-F axis of cytoarchitecture, we repeated all of the above analyses using the T1w/T2w ratio (fig. S1B) (23) and the principal gradient of functional connectivity (fig. S1C) (44) to define brain states. This is a

A Bottom-up state transitions required lower energy compared to top-down



B Cytoarchitectonic divergence correlates with larger energy asymmetries

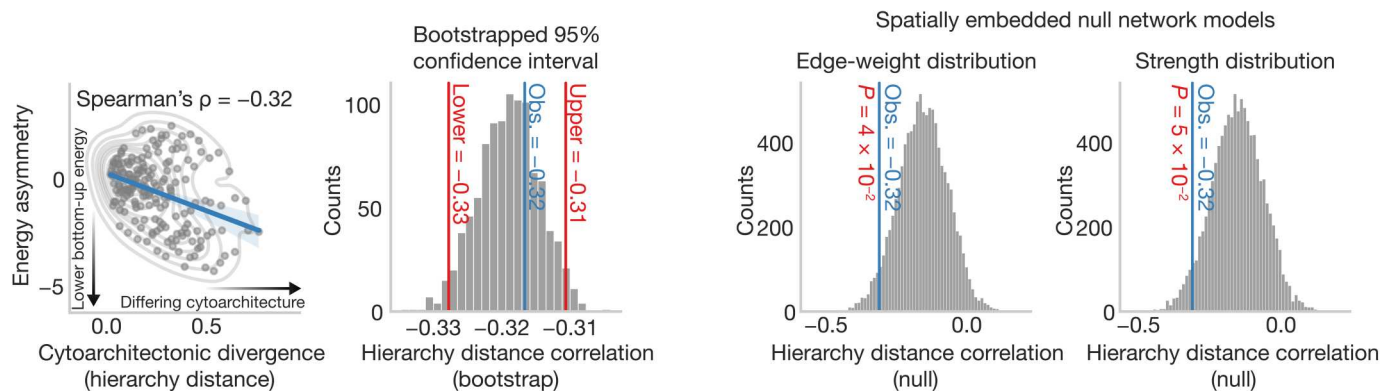


Fig. 2. The topology of the structural connectome is sensitive to asymmetries between top-down and bottom-up signal propagation across the S-F axis of cytoarchitecture. (A) Bottom-up energy was significantly lower than top-down energy (left), demonstrating that bottom-up state transitions were easier for our network control model to complete. One thousand bootstrapped resamples of the group-averaged connectome (see Materials and Methods) revealed that the 95% confidence interval (CI) of this asymmetry did not overlap 0. In addition, this mean asymmetry was larger than expected under a pair of null network models (right), including one that preserved the spatial embedding and the edge weight distribution of the network and another that preserved the spatial embedding and the strength distribution. (B) The distance along the cytoarchitectonic gradient separating the initial and target states was negatively correlated with energy asymmetries, demonstrating that high cytoarchitectonic dissimilarity between states was linked to greater negative energy asymmetries (left). This finding shows that when cytoarchitecture differs between brain states, bottom-up transitions required lower energy to complete compared to their top-down counterparts. The same bootstrap test described above revealed that the 95% CI of this correlation did not overlap 0. In addition, this correlation with hierarchy distance was larger than expected under the same pair of null network models described above (right). Together, these observations suggest that trans-hierarchical transition energy may be supported by the higher-order topology of the structural connectome.

relatively strong test of specificity as the gradient of cytoarchitecture was correlated with both the T1w/T2w ratio ($r = -0.68$) and the gradient of functional connectivity ($r = 0.56$). Using the T1w/T2w ratio, we found that neither the mean energy asymmetry (-0.11 , $P_{\text{edge}} = 0.699$, $P_{\text{strength}} = 0.707$; fig. S6A) nor the correlation with hierarchical distance ($\rho = 0.14$, $P_{\text{edge}} = 0.958$, $P_{\text{strength}} = 0.934$; fig. S6B) was larger than expected under our null network models. In addition, while energy asymmetries correlated significantly with diffusion efficiency asymmetry ($r = -0.31$, $P_{\text{FDR}} = 4 \times 10^{-5}$; fig. S6C) and search information asymmetry ($r = 0.23$, $P_{\text{FDR}} = 2 \times 10^{-3}$; fig. S6D), they no longer correlated significantly with our asymmetric measure of path transitivity ($r = 0.06$, $P_{\text{FDR}} = 0.420$; fig. S6E). A similar pattern of results was found for the functional connectivity gradient. Neither the mean energy asymmetry (0.15 , $P_{\text{edge}} = 0.943$, $P_{\text{strength}} = 0.900$; fig. S7A) nor the correlation with hierarchical

distance ($\rho = 0.11$, $P_{\text{edge}} = 0.906$, $P_{\text{strength}} = 0.844$; fig. S7B) was larger than expected under our null network models. Regarding the communicability metrics, energy asymmetries were significantly correlated with diffusion efficiency asymmetry ($r = -0.58$, $P_{\text{FDR}} = 3 \times 10^{-18}$; fig. S7C) and search information asymmetry ($r = 0.55$, $P_{\text{FDR}} = 4 \times 10^{-16}$; fig. S7D) but not transitivity ($r = 0.09$, $P_{\text{FDR}} = 0.215$; fig. S7E).

These results indicate that asymmetries between bottom-up and top-down transition energies were stronger for the S-F axis of cytoarchitecture compared to both the T1w/T2w ratio and the principal gradient of functional connectivity. Specifically, only energy asymmetries for the S-F axis revealed a clear hierarchy distance effect and a correlation with cumulative path transitivity. This result may be explained by the fact that these axes diverge at their apexes (3, 53). For example, the top of the S-F axis comprises

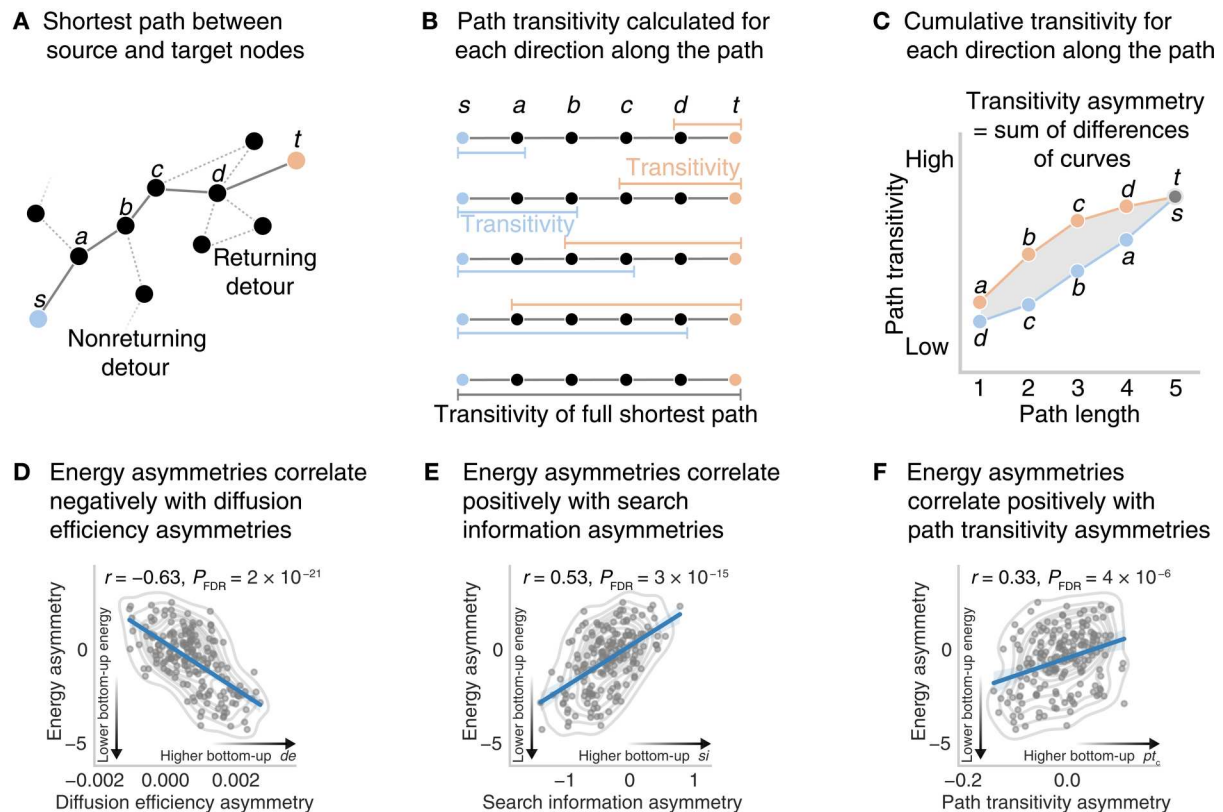


Fig. 3. Asymmetries in transition energy are explained by asymmetries in communicability. We examined how our energy asymmetries correlated with asymmetries in diffusion efficiency, search information, and path transitivity. While diffusion efficiency and search information represent asymmetric communicability metrics, path transitivity is symmetric. Thus, we defined a modified version of path transitivity that was sensitive to asymmetries in the human connectome. (A) Path transitivity measures the occurrence of returning detours (i.e., triangles) along a given shortest path. Path transitivity is typically estimated along the entire length of the shortest path and is symmetric. (B) We modified path transitivity by estimating it separately for each segment of the shortest path starting from nodes located at either end. (C) Doing so allowed us to estimate a pair of cumulative path transitivity curves: one for each direction along the shortest path. These curves allowed us to probe whether returning detours were encountered sooner in one direction or the other, which we quantified by subtracting the curves and summing the differences. (D) Energy asymmetries correlated negatively with asymmetries in diffusion efficiency. Thus, lower bottom-up energy corresponds to higher bottom-up diffusion efficiency. (E) Energy asymmetries correlated positively with asymmetries in search information. Thus, lower bottom-up energy corresponds to lower bottom-up search information. (F) Energy asymmetries correlated positively with asymmetries in cumulative path transitivity. Thus, lower bottom-up energy corresponds to lower bottom-up path transitivity; in turn, returning detours are encountered sooner for top-down signaling.

paralimbic regions, while the top of the functional connectivity axis comprises the transmodal cortex. Previous work has suggested that this (relative) untethering of functional connectivity from cytoarchitectonic constraints may support the functional diversity of the transmodal cortex (3). This untethering is also consistent with evidence that macroscopic structural and functional connectivity are relatively uncoupled in the transmodal cortex compared to the unimodal cortex (54, 55). Thus, our findings converge on the idea that while cytoarchitecture and structural connectivity are tightly intertwined, functional connectivity departs from both in a spatially patterned way. In addition, our results indicate that although the S-F axis and T1w/T2w ratio are correlated, they show marked differences that may be critical to capturing how brain structure constrains connectivity.

The gradient of cytoarchitecture constrains the flow of activity over the cortex

The above findings demonstrate that the energy asymmetries associated with trans-hierarchical state transitions may result from a

topology wired to propagate activity up the cytoarchitectonic gradient more efficiently compared to down. To illustrate this phenomenon intuitively, we examined whether the flow of uncontrolled activity followed the S-F axis as it spread throughout the cortex over time (see Materials and Methods). Briefly, seeding from each brain state, we examined the spread of natural dynamics across the whole brain as they unfolded over time. This amounted to resimulating our dynamical model for each initial state in the absence of both a target state and a control set. Below, we used this approach to show that the activity in our diffusive model preferentially propagates up the S-F axis.

For each seed brain state and time point, t , we calculated the Spearman's rank correlation between the pattern of simulated activity at each node and the S-F axis (Fig. 4A). Note that this correlation was computed excluding the regions that made up a given seed state (i.e., where activity was propagating from). Thus, correlations were not driven by activity leaving a given brain state. For a given time step, negative correlations indicated that brain activity was higher at the bottom of the hierarchy than at the top, while positive

A Uncontrolled dynamics

Uncontrolled simulated activity spreading throughout the cortex over time (t) seeded from a specific state (●)

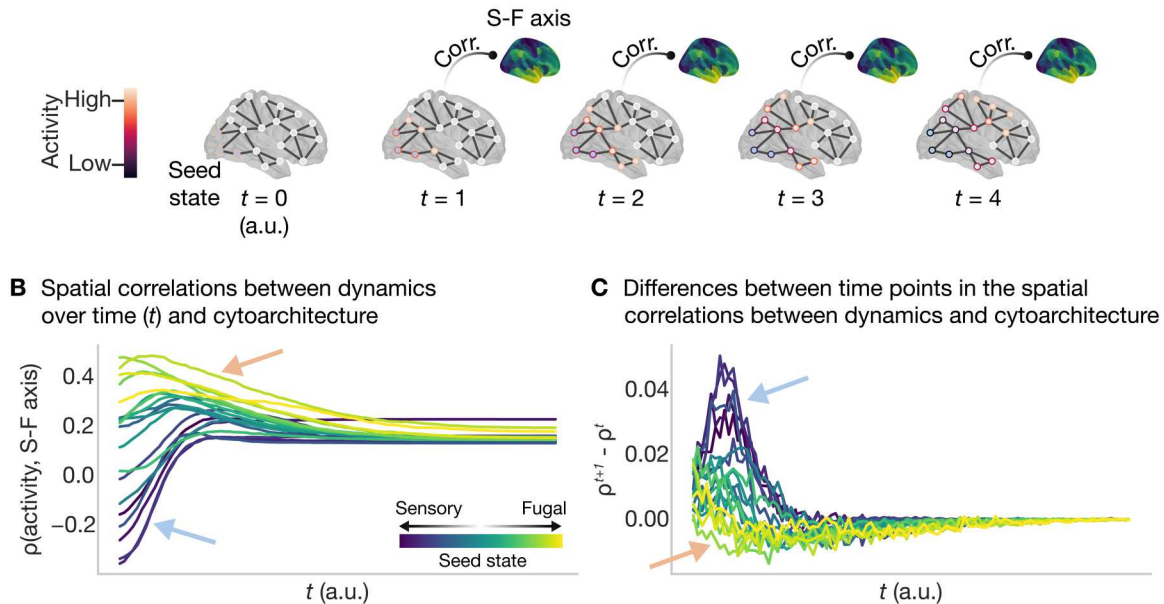


Fig. 4. Uncontrolled dynamics preferentially flow up the cortical gradient of cytoarchitecture. (A) We simulated the spread of uncontrolled dynamics seeded from each of our cytoarchitectonic brain states and tracked the activity as it unfolded over time and spread throughout the cortex. For a given seed state, we quantified the Spearman rank correlation between the S-F axis of cytoarchitecture and the pattern of simulated activity at time t as well as the difference in correlations between adjacent time points. (B) Correlations between cytoarchitecture and simulated activity seeded from each brain state as a function of time. Negative correlations indicate that brain activity at time t was higher at the bottom of the hierarchy than at the top, while positive correlations indicate the opposite. States lower on the hierarchy tend to show negative correlations between the S-F axis and early activity propagation (blue arrow), while states higher on the hierarchy tend to show positive correlations (peach arrow). (C) Differences in correlations between neighboring time points as a function of time. These low-hierarchy negative correlations diminish more quickly (blue arrow), by becoming less negative, compared to the positive correlations in high-hierarchy states (peach arrow). Collectively, these results suggest that uncontrolled dynamics spread more readily across the S-F axis in the bottom-up direction than top-down.

correlations indicated the opposite. Figure 4B shows that states lower on the hierarchy tend to show negative correlations between the S-F axis and early activity propagation (Fig. 4B, blue arrow), while states higher on the hierarchy tend to show positive correlations (Fig. 4B, peach arrow). This pattern demonstrates that early signal propagation tends to activate regions near to a state's location on the hierarchy. That is, activity propagating from low positions on the hierarchy reaches other low-hierarchy regions first, driving a negative correlation, while activity propagating from high on the hierarchy reaches other high-hierarchy regions first, driving a positive correlation. Critically, Fig. 4B also shows that the negative correlations low on the hierarchy diminish (i.e., become less negative) more quickly compared to the positive correlations for the high-hierarchy states. This effect is quantified and recapitulated in Fig. 4C, which shows the differences in correlations between neighboring time points ($\rho^{t+1} - \rho^t$). We found that differences in correlations between time points were greater when activity was seeded from the bottom of the hierarchy (Fig. 4C, blue arrow) compared to the top (Fig. 4C, peach arrow). These results suggest that activity propagates more readily in the bottom-up direction than in the top-down direction. Furthermore, these results are consistent with our observation of lower bottom-up energy compared to top-down (see Fig. 2); a topology that is organized to facilitate

bottom-up activity flow will require less energy to complete controlled bottom-up state transitions compared to top-down.

Energy asymmetries in trans-hierarchical state transitions are correlated with differences in intrinsic time scales and asymmetries in effective connectivity

Our observations thus far are consistent with the notion that regional cytoarchitectonic similarity influences the difference between bottom-up and top-down signal propagation across the cortical hierarchy. Specifically, our results suggest that how patterns of brain activity spread across the hierarchy varies as a function of the direction of flow. However, the results presented thus far were only derived from linear dynamics simulated upon the structural connectome. We reasoned that if our results for simulated dynamics were neurobiologically meaningful, then we would observe two findings.

First, we expected that energy asymmetries would correlate with changes in the intrinsic neuronal time scales of our brain states. Specifically, we predicted that transitions where bottom-up energy was lower than top-down would correspond to a lengthening of neuronal time scales between the initial and target states. In turn, this finding would suggest that the topology of the structural connectome is wired to support the integration of information that is thought to be occurring as activity traverses up the hierarchy.

Second, we expected that energy asymmetries would be consistent with asymmetries derived from dynamical models trained on functional neuroimaging data. To test the former prediction, we used open-access human electrocorticography (ECoG) data (56) to index regions' intrinsic time scales. Specifically, following Gao *et al.* (24), we quantified time scales using the time constant, τ , of an exponential decay function fitted to the autocorrelation function of the ECoG time series (Fig. 5A; see Materials and Methods). Larger τ values correspond to longer (slower) fluctuations in a region's intrinsic time scales. Subsequently, we averaged τ within each of our brain states and then subtracted the mean τ between pairs of brain states, τ_{Δ} . Thus, positive τ_{Δ} represented a larger τ in state j compared to that in state i . Last, we correlated T_{EA} with τ_{Δ} and found that they were negatively correlated (Fig. 5B). This result indicates that state transitions where bottom-up energy is lower than top-down (i.e., negative T_{EA}) are also characterized by an increase in τ (i.e., positive τ_{Δ}) going from state i to state j and vice versa. Thus, state transitions that are (relatively) easy to complete are coincident with a lengthening of the time scales of resting-state electrophysiological fluctuations.

Next, we turned from an evaluation of differences between brain states' intrinsic neuronal time scales to an evaluation of asymmetries derived from effective connectivity (EC). Specifically, we computed the EC between brain states using a spectral version of dynamic causal modeling (spDCM) (57) applied to participants' resting-state functional magnetic resonance imaging (rs-fMRI) data (see Materials and Methods). We subsequently computed EC asymmetries by subtracting top-down EC from bottom-up EC ($EC_{\Delta} = |EC| - |EC|^T$). We found that T_{EA} was positively correlated with EC_{Δ} ($r = 0.24$, $P = 1 \times 10^{-3}$; fig. S8), indicating that for state transitions where bottom-up energy was lower than top-down, the same was true for EC and vice versa. This result extends prior work (43) by demonstrating that the topology of the undirected structural connectome supports directed signal propagation along the cortical gradient of cytoarchitectonic similarity.

Optimized control weights track the S-F axis of cytoarchitecture and increase energy asymmetries

The preceding sections demonstrated that brain network topology may be wired to facilitate more efficient bottom-up trans-

hierarchical state transitions compared to top-down and that this effect (i) is not better explained by spatial embedding or lower-order topology, (ii) may be specific to cytoarchitecture, and (iii) is consistent with asymmetries in intrinsic time scales and EC. These findings were also supported by results from internodal communicability metrics, suggesting that how patterns of brain activity spread across the hierarchy varies as a function of the direction of flow. However, while convergence with communicability provides deeper insight into our results, a relative strength of NCT lies in its capacity to not only simulate dynamics but also to control them. In this section, we sought to leverage this strength by studying whether the regions' position along the S-F axis informed their capacity to facilitate trans-hierarchical state transitions.

To achieve the above goal, we optimized state transitions by introducing a variable set of control weights using a data-driven approach (see Materials and Methods). Briefly, for each state transition, we systematically perturbed the system to generate a set of control weights that minimized transition energy (Fig. 6A). Rather than assuming that all regions have equal influence over dynamics, these weights tune the control assigned to different brain regions with the goal of reducing transition energy (i.e., improving the efficiency of state transitions). For each state transition, we examined the correlation between these optimized control weights and the hierarchical distance separating nodes from the associated initial/target state (see Materials and Methods). We assigned P values using Brain Surrogate Maps with Autocorrelated Spatial Heterogeneity (BrainSMASH) (58) and corrected for multiple comparisons via the Benjamini and Hochberg false discovery rate (FDR; $q = 0.05$) procedure (59). Here, any observed correlation implies that optimizing control weights uncovers a spatial mode of control variation that tracks the gradient of cytoarchitecture. Last, we examined how optimized control weights influenced energy asymmetries. Here, we computed the absolute mean T_{EA} for both uniform and optimized control weights using 1000 bootstrapped re-samples of the group-averaged connectome (see Materials and Methods).

We found that optimized weights correlated negatively with nodes' hierarchical distance from the initial/target states (Fig. 6B). This result shows that optimized control weights reduce as nodes traverse along the S-F axis away from the initial/target states.

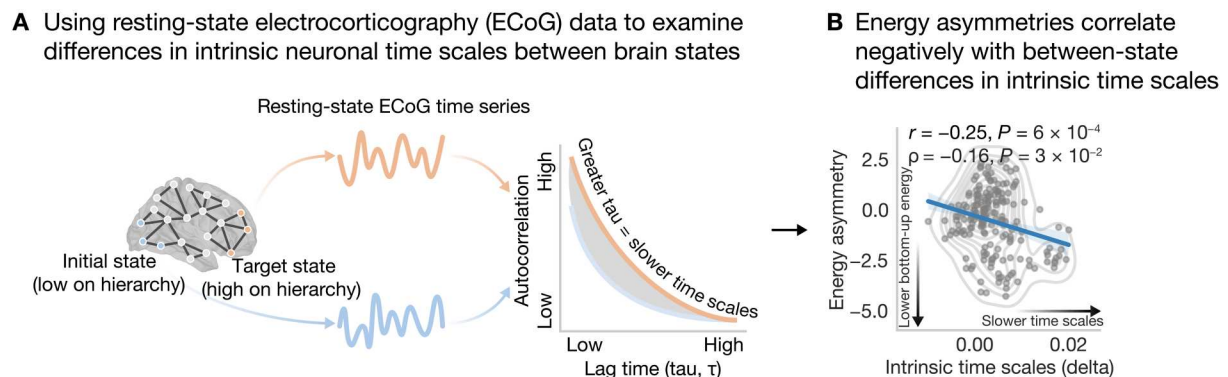
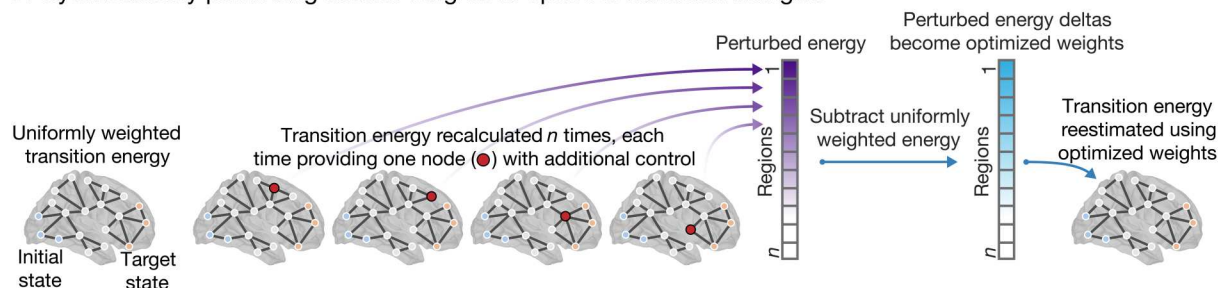
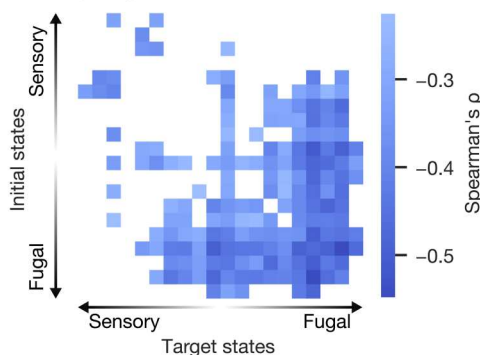


Fig. 5. Energy asymmetries correlate with differences between brain states' intrinsic neuronal time scales. (A) We used resting-state ECoG data to examine differences between brain states' intrinsic neuronal time scales [as per methods described by Gao *et al.* (24)] between our cytoarchitectonic brain states. (B) Energy asymmetries between brain states were negatively correlated with differences between brain states' intrinsic time scales. This result shows that state transitions where bottom-up energy is lower than top-down (negative energy asymmetry) are also characterized by a slowing of intrinsic time scales going from state i to state j and vice versa.

A Systematically perturbing control weights to optimize transition energies



B Optimized weights decay as a function of distance from initial/target states along the sensory-fugal axis



C Absolute energy asymmetries are larger for optimized control weights compared to uniform control weights

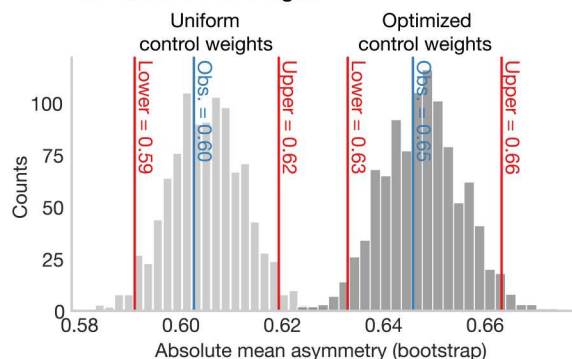


Fig. 6. Optimized control weights track the cortical gradient of cytoarchitecture and maximize energy asymmetries. (A) For each trans-hierarchical state transition, we adopted the following procedure to generate optimized control weights that minimized transition energy. First, for a given state transition, we calculated uniformly weighted transition energy; nodes of the system were provided the same degree of control over system dynamics. Note that the results for uniformly weighted transition energy have been reported in all figures before this one. Second, we reestimated the transition energy n times, each time providing one node with additional control over the system. This approach generated a vector of perturbed transition energies (purple vector). Third, we subtracted the uniformly weighted energy from each of the perturbed energies to generate a vector of perturbed energy delta values (blue vector), the magnitude of which encoded the regions' importance to the state transition. Fourth, we reestimated transition energy one more time using the perturbed energy deltas as optimized control weights. (B) Correlations between optimized control weights for each state transition and the S-F axis. For each state transition, we estimated the Spearman rank correlation between the nodes' optimized weights and their distance along the S-F axis from the initial and target state and retained whichever correlation was strongest (see Materials and Methods). BrainSMASH P values were corrected for multiple comparisons using the Benjamini-Hochberg FDR (59). Significance was determined as $P_{FDR} < 0.05$. We found that optimized weights correlated negatively with hierarchical distance, indicating that they decayed as a function of distance from the initial/target state. (C) Mean energy asymmetries ($|T_{EA}|$) for uniform (light gray) compared to optimized (dark gray) control weights under 1000 bootstraps (see Materials and Methods). Mean $|T_{EA}|$ was larger for optimized control weights compared to uniform control weights. Thus, optimizing control weights maximized energy asymmetries.

Thus, optimized weights track the gradient of cytoarchitecture, and this tracking exceeds that which would be expected on the basis of the spatial autocorrelation embedded in the data. Next, we found that the mean energy asymmetry (T_{EA}) was larger for optimized control weights compared to uniform control weights (Fig. 6C). Note that optimized weights were only designed to minimize transition energy, including both bottom-up and top-down energies. Thus, this observed increase in mean energy asymmetry suggests that our data-driven optimized control weights minimized bottom-up energy to a greater extent than top-down. Together, these results illustrate that a region's position along the S-F axis explains its role in facilitating trans-hierarchical state transitions and that imbuing our model with knowledge of these roles optimizes the efficiency of bottom-up signal propagation across the hierarchy.

Asymmetries in trans-hierarchical state transitions are refined throughout development

Having illustrated that a region's position along the S-F axis explains its role in facilitating state transitions, in this final section, we sought to characterize the developmental trajectories of transition energies. On the basis of previous literature, we expected that ongoing developmental refinement of structural connectivity would result in age-related changes to bottom-up and top-down energy. To test this expectation, we estimated the correlation between participant-specific transition energies and age while controlling for sex, total brain volume, edge density, and in-scanner motion (Fig. 7A). Here, energy was estimated using participant-specific optimized weights (see Materials and Methods and the previous section). Next, for each participant, we averaged transition energies over bottom-up and top-down transitions separately and subtracted the mean values to get participant-specific energy asymmetries. We found that age correlated positively with these energy asymmetries

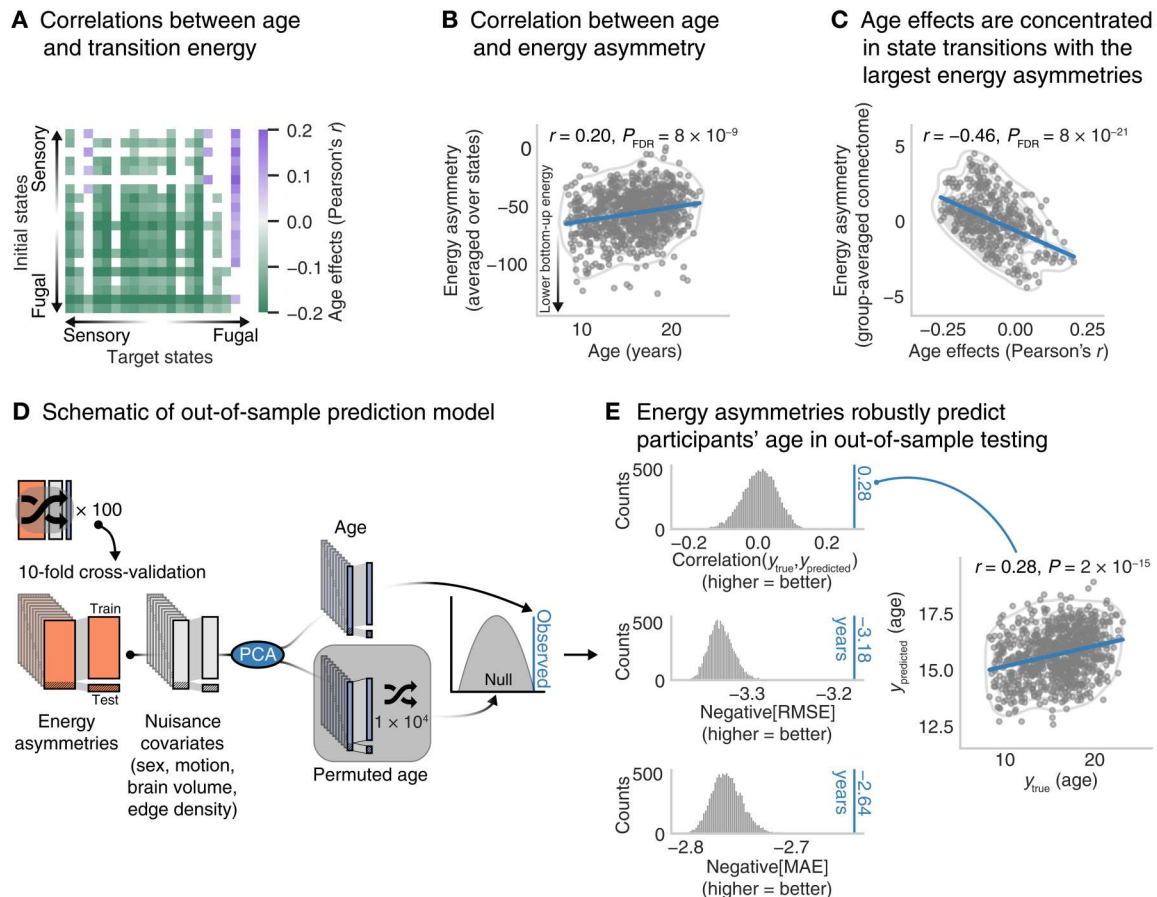


Fig. 7. Energy asymmetries in trans-hierarchical state transitions vary systematically over development. We estimated correlations between age and trans-hierarchical transition energy in 793 individuals while controlling for sex, total brain volume, edge density, and in-scanner motion. (A) Correlations between age and transition energy for all state transitions. We observed widespread negative correlations between age and transition energy, suggesting that state transitions became easier to complete as individuals got older. (B) Correlation between age and participant-specific energy asymmetries averaged over bottom-up and top-down state transitions. We found a positive correlation between age and energy asymmetries, indicating that the energy asymmetries between bottom-up and top-down closed throughout youth. (C) Correlation between age effects for individual state transitions [from (A)] and the energy asymmetries derived from the group-averaged structural connectome ($T_{E\Delta}$; see Fig. 2). We found that the age effects (Pearson's r) were negatively correlated with $T_{E\Delta}$, demonstrating that the strongest age effects were concentrated in the state transitions with the largest energy asymmetries. (D) Schematic illustration of a cross-validated regression model that was used to assess the out-of-sample prediction of participants' age. (E) Results from the out-of-sample prediction of participants' age. Energy asymmetries robustly predicted the participants' age in out-of-sample testing when scored using the correlation between true and predicted y (top left), negative root mean square error (middle left), and negative MAE (bottom left). As both error metrics represent the original units of y , these results show that our model was able to predict age to within 2.64 to 3.18 years. Note that these prediction effects were replicated when using both a higher-resolution version of our parcellation that included 400 parcels [Schaefer 400; correlation(y_{true} , $y_{predicted}$) = 0.30; negative[RMSE] = -3.15; negative[MAE] = -2.60] and a 360-parcel multimodal parcellation developed in the Human Connectome Project [correlation(y_{true} , $y_{predicted}$) = 0.30; negative[RMSE] = -3.15; negative[MAE] = -2.61]. Together, these results show that asymmetries in trans-hierarchical signal propagation and neurodevelopment are intimately intertwined.

(Fig. 7B). This effect was driven by the fact that the correlation between age and top-down energy ($r = -0.24$, $P_{FDR} = 7 \times 10^{-12}$; fig. S9A) was stronger than that observed for bottom-up energy ($r = -0.09$, $P_{FDR} = 1 \times 10^{-2}$; fig. S9B). Thus, while top-down and bottom-up energy both decreased throughout development, top-down energy did so more quickly. In turn, energy asymmetries weakened as a function of age. These results suggest that neurodevelopmental refinement of the connectome may involve converging toward a balance between bottom-up and top-down signal propagation. We also found that the age effects for individual transitions (from Fig. 7A) were negatively correlated with the energy asymmetries taken from the group-average connectome (Fig. 7C). This

result demonstrates that state transitions with stronger energy asymmetries in the group-averaged connectome also showed the strongest age effects. Lastly, using a cross-validated penalized regression model (Fig. 7D; see Materials and Methods), we found that energy asymmetries were able to robustly predict participants' age in out-of-sample testing (Fig. 7E; see also fig. S10 that shows that optimized energies better predicted participants' age compared to nonoptimized energies derived from uniform control weights). Consistent with our expectations, these results show that development plays a critical role in refining trans-hierarchical transition energies and that this refinement is concentrated in state transitions with divergent cytoarchitecture.

DISCUSSION

Here, we investigated how the relationship between cytoarchitecture and connectivity constrains the dynamics supported by the structural connectome. Using NCT (45, 46, 60, 61), we modeled the amount of control energy that was required to propagate linear dynamics up and down the S-F axis of cytoarchitecture. We reported several key findings. First, we found that the energy required to complete bottom-up state transitions was lower compared to their top-down counterparts, indicating that bottom-up transitions were easier for our model to complete. In addition, through a combination of null network models, as well as analyses of communicability and uncontrolled dynamics, we found that this energy asymmetry was underpinned by a network topology that is wired to enable efficient bottom-up signaling across the cortical hierarchy. Second, we found that energy asymmetries correlated with differences in intrinsic neuronal time scales estimated from ECoG and asymmetries in EC estimated from rs-fMRI. The former finding demonstrates that efficient bottom-up signaling across the structural connectome is coincident with a lengthening of regions' temporal receptive windows, while the latter shows that our model of dynamics is consistent with those drawn from functional data. Third, we found that the regions' position along the S-F axis was correlated with their importance in facilitating state transitions, demonstrating that the spatial modes of control embedded in our model were coupled to the cortical hierarchy. Last, we found that asymmetries between bottom-up and top-down energy decreased as a function of age in a sample of developing youths. Overall, our results demonstrate that the higher-order topology of the human connectome may be wired to support asymmetric signaling across the cortical hierarchy and that this signaling is rooted in the spatial patterning of cytoarchitecture that is itself guiding the ongoing refinement of connectivity throughout youth.

Cytoarchitecture shapes the connectome

Understanding how cytoarchitecture shapes connectivity is a central goal of neuroscience (62). In humans, recent research has shown a clear link between cortical cytoarchitecture and local properties of structural connectivity (25, 47, 63). Using graph theory, Wei *et al.* (25) found that several indices of regions' local network importance correlated moderately with regions' cytoarchitectonic similarity to the rest of the brain, demonstrating that regions with similar cytoarchitecture were more strongly and more globally connected to the rest of the network. Paquola *et al.* (47) defined a regional embedding space that fused together edge-level structural connectivity, geodesic distance, and cytoarchitectonic similarity (3). Paquola *et al.* (47) found that their wiring diagram explained variance in regional externopyramidization—which tracks the laminar origin of neuronal projections (62)—supporting the notion that variance in the laminar origin of feedback and feedforward connections is intertwined with variance in cytoarchitecture and macroscopic connectivity. Our findings extend these prior studies by showing that cytoarchitecture shapes not only the local connectivity but also the higher-order topology of the structural connectome. Specifically, our findings suggest that cytoarchitecture may constrain the traversal of structural pathways to engender efficient bottom-up signal routing over the hierarchy. Thus, it appears that cytoarchitecture predicts not only which pairs of regions are connected [i.e., “like connects with like,” cf. the structural model

(1, 2, 18, 20)] but also the spatial embedding of senders and receivers in the brain (43, 64, 65).

To probe potential explanations for how cytoarchitecture constrains higher-order topology, we examined three asymmetric communicability metrics (43, 50–52): diffusion efficiency, search information, and cumulate path transitivity. We found that lower bottom-up transition energy was associated with higher bottom-up diffusion efficiency, lower bottom-up search information, and lower bottom-up cumulative path transitivity. The first two correlations indicate the intuitive result that bottom-up energy may be lower because bottom-up diffusion of activity is more efficient—a conclusion that is also supported by our analysis of uncontrolled dynamics—and because it is more likely to track the shortest paths. The correlation with cumulative path transitivity indicates that top-down signaling encounters a greater number of returning detours nearer to the top of the S-F axis. In our model, the presence of local detours creates cycles that may give rise to sustained activity patterns (66). In turn, the early occurrence of these detours may result in the earlier onset of sustained activity patterns for top-down state transitions. Thus, higher top-down energy may reflect the increased effort required to propagate these recurrent activity patterns down the S-F axis. This interpretation is consistent with the idea that the apex of the S-F axis forms a limbic workspace, wherein sustained activity patterns support ongoing prediction and integration of sensory signals in a predictive coding framework (67).

Energy asymmetries link to changes in intrinsic neuronal time scales and EC

Recent work has shown that the spatial patterning of regions' intrinsic neuronal time scales correlates with the patterning of the T1w/T2w ratio (24), suggesting that the brain's time scale hierarchy reflects its cytoarchitectonic hierarchy. Here, we found that the asymmetries in trans-hierarchical state transitions were coupled to differences in state-level intrinsic neuronal time scales. Specifically, the easier a bottom-up state was to complete (compared to its top-down counterpart), the more the time scale of the target state lengthened compared to the initial state. Lengthening time scales are thought to be associated with progressive changes to longer temporal receptive windows, which, in turn, are thought to underpin shifts from segregated to integrated functional processing (68). Thus, convergent with our communicability results, these findings show that the topology of the structural connectome may be wired to support the progressive integration of lower-order properties of our environment into higher-order percepts and cognitions. Our findings also serve as a functional validation of our network control model; we observed a positive correlation between energy asymmetries and asymmetries in EC, which is consistent with past literature (43). Thus, our findings contribute to a growing body of evidence demonstrating that asymmetric signal routing is measurable from the topology of the connectome, despite being derived from an undirected description of brain connectivity.

Energy asymmetries refine systematically throughout youth

The effects of development on connectome topology are increasingly well studied (35, 69–71), including with NCT where the amount of control energy required to activate the executive function system (from baseline) has been shown to decrease throughout youth (72).

This observation is consistent with the current study, wherein the energy associated with trans-hierarchical state transitions also reduced throughout youth. Here, we provide a key extension to prior work that deepens our understanding of these developmental energy effects; we observed that energy asymmetries diminished as a function of age in our sample and that this effect was driven by stronger age effects for top-down energy compared to bottom-up. These findings suggest that maturation throughout youth alters the balance between bottom-up and top-down signal propagation, refining the connectome toward an equilibrium between the two. This interpretation is consistent with a staging account of neurodevelopment that suggests that lower-order connections are refined earlier in development compared to their higher-order counterparts (1, 32–34). That is, the energy asymmetry that we observed might reflect the relatively advanced refinement of lower-order connections that is already well underway by 8 years of age (the youngest in our sample). In turn, the stronger age effect observed for top-down energy might reflect the relatively delayed onset of refinement of higher-order connections that may be occurring within the age range of our sample. Examining how our results present on either side of the age range of the PNC, as well as whether they are supported by longitudinal data, will be a critical avenue for future research.

Despite the strengths of this study, we note several limitations. Similar to our recent work (73), a limitation of this study is the use of a linear model of neuronal dynamics to estimate signal propagation across the S-F axis. While this assumption is an oversimplification of brain dynamics, linear models explain variance in the slow fluctuations in brain activity recorded by fMRI (74, 75), suggesting that they successfully approximate the kinds of data commonly used to examine brain function. An additional limitation is the use of a single map of cytoarchitecture to define brain states, which precluded us from defining participant-specific states. This limitation may be compounded by the fact that the S-F axis that we used was obtained from an adult brain, whereas our structural connectomes were estimated in a developing sample. As mentioned above, previous work contends that the T1w/T2w ratio forms a reasonable proxy of the S-F axis that is measurable in vivo (3). However, while the PNC includes T1-weighted imaging, it does not include T2-weighted imaging (48), which prevented us from estimating the T1w/T2w ratio in our sample. Replication of our findings using participants' T1w/T2w maps is warranted given the well-known individual variability in the spatial patterning of cortical structural features. However, this approach must be weighed against the fact the T1w/T2w ratio is imperfectly correlated with the S-F axis. Thus, such replication efforts must consider the trade-off between the value of capturing individual variability and the cost of potentially disconnecting from the relevant underlying neurobiology (i.e., cytoarchitecture). Our results showing that energy asymmetries did not replicate using the T1w/T2w ratio taken from the Human Connectome Project data support this interpretation. Last, our use of a developmental sample limits the generalizability of our findings beyond the age range of the PNC. Future work may consider replicating our effects in life-span data to examine the extent to which energy asymmetries are a general feature of connectome organization. This is particularly pertinent given recent work showing protracted changes to the rich club of the connectome across 5 to 80 years of age (76).

Together, our results demonstrate that cytoarchitecture may constrain network topology in such a way as to induce asymmetries in signal propagation across the cortical hierarchy. Specifically, we found that bottom-up trans-hierarchical state transitions were easier to complete than their top-down counterparts, that energy asymmetries correlated with asymmetries in communicability metrics and changes to neuronal time scales, that control signals tracked the S-F axis, and that asymmetries reduced with age in youth. Collectively, our work highlights that variation in the properties of cortical microstructure that govern extrinsic connectivity may guide the formation of macroscopic connectome topology.

MATERIALS AND METHODS

Participants

Participants included 793 individuals from the PNC (48), a community-based study of brain development in youths aged 8 to 22 years. The institutional review boards of both the University of Pennsylvania and the Children's Hospital of Philadelphia approved all study procedures. The neuroimaging sample of the PNC consists of 1601 participants. From this original sample, 156 were excluded due to the presence of gross radiological abnormalities distorting brain anatomy or due to a medical history that might affect brain function. Next, a further 159 participants were excluded because they were taking psychoactive medication at the time of study. An additional 466 individuals were excluded because they did not pass rigorous manual and automated quality assurance for their T1-weighted scan (77), their diffusion scan (78), or their rs-fMRI scan (79). Lastly, 27 participants were excluded owing to the presence of disconnected regions in their structural connectivity matrix (see the "Structural connectome construction" section). This process left a final sample of 793 participants.

Imaging data acquisition

MRI data were acquired on a 3-T Siemens Tim Trio scanner with a 32-channel head coil at the Hospital of the University of Pennsylvania. Diffusion-weighted imaging (DWI) scans were acquired via a twice-refocused spin-echo, single-shot echo-planar imaging sequence (repetition time = 8100 ms, echo time = 82 ms, and field of view = 240 mm²/240 mm²; matrix: RL: 128, AP: 128; slices, 70; in-plane resolution of 1.875 mm²; slice thickness = 2 mm, gap = 0; flip angle = 90°/180°/180°, 71 volumes, GRAPPA factor = 3, bandwidth = 2170 Hz/pixel, and phase-encoding direction = anterior-posterior). The sequence used a four-lobed diffusion encoding gradient scheme combined with a 90-180-180 spin-echo sequence designed to minimize eddy-current artifacts. The sequence consisted of 64 diffusion-weighted directions with $b = 1000$ s/mm² and seven interspersed scans where $b = 0$ s/mm². The imaging volume was prescribed in axial orientation and covered the entire brain.

In addition to the DWI scan, a B0 map of the main magnetic field was derived from a double-echo, gradient-recalled echo sequence, allowing for the estimation and correction of field distortions. Before DWI acquisition, a 5-min magnetization-prepared, rapid acquisition gradient-echo T1-weighted image (TR = 1810 ms, TE = 3.51 ms, FOV = 180 mm by 240 mm, matrix of 256 × 192, and effective voxel resolution of 0.94 mm by 0.94 mm by 1 mm) was acquired for each participant.

Last, approximately 6 min of rs-fMRI data was acquired using a blood oxygen level-dependent (BOLD-weighted) sequence

(TR = 3000 ms, TE = 32 ms, FOV = 192 mm by 192 mm, resolution 3 mm isotropic, and 124 volumes). These data were used primarily to generate the principal cortical gradient of functional connectivity (see the “Alternative hierarchies” section) (44).

Imaging data quality control

All DWI and T1-weighted images underwent rigorous quality control by highly trained image analysts [see (78) and (77) for details on DWI and T1-weighted imaging, respectively]. Regarding the DWI acquisition, all 71 volumes were visually inspected and evaluated for the presence of artifacts. Every volume with an artifact was marked as contaminated, and the fraction of contaminated volumes was taken as an index of scan quality. Scans were marked as “poor” if more than 20% of volumes were contaminated, “good” if more than 0% but less than 20% of volumes were contaminated, and “great” if 0% of volumes were contaminated. Regarding the T1-weighted acquisition, images with gross artifacts were considered “unusable”; images with some artifacts were flagged as “usable”; and images free of artifact were marked as “superior.” As mentioned above in the “Participants” section, 466 individuals were removed because of quality. Of these, 318 individuals were removed because of either poor DWIs or unusable T1-weighted images. In the final sample of 793 participants, a total of 535 participants had diffusion tensor images identified as great, with the remaining identified as good, and 701 participants had T1-weighted images identified as superior, with the remaining identified as usable. Regarding the rs-fMRI data, the remaining 148 of the 466 excluded participants were removed either because their mean relative root mean square framewise displacement was higher than 0.2 mm or because their scan included more than 20 frames with motion exceeding 0.25 mm.

Structural image processing

Structural image processing was carried out using tools included in Advanced Normalization Tools (ANTs) (80). The buildtemplateparallel pipeline from ANTs (81) was used to create a study-specific T1-weighted structural template with 120 participants that were balanced on sex, race, and age. Structural images were processed in participants’ native space using the following procedure: brain extraction, N4 bias field correction (82), Atropos tissue segmentation (83), and SyN diffeomorphic registration (81, 84).

Diffusion image processing

For each participant, a binary mask was created by registering the standard fractional anisotropy mask provided by FSL (FMRIB58 FA) to the participant’s mean $b = 0$ reference image using FLIRT (85). To correct for eddy currents and head motion, this mask and the participant’s diffusion acquisition were passed to FSL’s eddy (version 5.0.5) (86). Diffusion gradient vectors were subsequently rotated to adjust for the motion estimated by eddy. Distortion correction was conducted via FSL’s FUGUE (87) using the participant’s field map, estimated from the B0 map.

rs-fMRI processing

State-of-the-art processing of functional data is critical for valid inference (88). Thus, functional images were processed using a top-performing preprocessing pipeline implemented using the eXtensible Connectivity Pipeline Engine (79), which includes tools from FSL (87, 89) and AFNI (90). This pipeline included (i) correction

for distortions induced by magnetic field inhomogeneity using FSL’s FUGUE utility, (ii) removal of four initial volumes, (iii) realignment of all volumes to a selected reference volume using FSL’s MCFLIRT, (iv) interpolation of intensity outliers in each voxel’s time series using AFNI’s 3dDespike utility, (v) demeaning and removal of any linear or quadratic trends, and (vi) coregistration of functional data to the high-resolution structural image using boundary-based registration. Images were denoised using a 36-parameter confound regression model that has been shown to minimize associations with motion artifact while retaining signals of interest in distinct subnetworks (79, 91). This model included the six framewise estimates of motion, the mean signal extracted from eroded white matter and cerebrospinal fluid compartments, the mean signal extracted from the entire brain, the derivatives of each of these nine parameters, and the quadratic terms of each of the nine parameters and their derivatives. Both the BOLD-weighted time series and the artifactual model time series were temporally filtered using a first-order Butterworth filter with a passband of 0.01 to 0.08 Hz (92).

Imaging-derived nuisance covariates

In our analyses of individual differences, we used total brain volume, edge density, and mean in-scanner motion as imaging-derived nuisance covariates. Total brain volume was generated from the T1-weighted images using ANTs. In-scanner head motion was estimated for each participant from their DWI sequence as relative framewise displacement (78). Specifically, rigid-body motion correction was applied to the seven high-quality $b = 0$ images interspersed throughout the diffusion acquisition. Once estimated, framewise displacement was averaged across time to create a single measure for each participant. Edge density was estimated from each participant’s adjacency matrix (see the “Structural connectome construction” section) as the fraction of present connections to all possible connections.

Structural connectome construction

For each participant, whole-brain deterministic fiber tracking was conducted using DSI Studio (93) with a modified fiber assessment by continuous tracking algorithm with Euler interpolation. A total of 1,000,000 streamlines were generated for each participant that were between 10 and 400 mm long. Fiber tracking was performed with an angular threshold of 45° and step size of 0.9375 mm. Next, following our previous work (73), the number of streamlines intersecting region i and region j in a 200-parcel cortical parcellation (94) was used to weight the edges of an undirected adjacency matrix, A [see fig. S11 for sensitivity analyses covering different parcellation resolutions and definitions (95)]. Note that $A_{ij} = 0$ for $i = j$. This process yielded 793 subject-specific A matrices that were used in subject-level analyses reported in the main text (i.e., Fig. 6). Our primary analyses, however, were based on a group-averaged A matrix. To obtain this A matrix, we averaged over the entries of the individuals’ A matrices and thresholded using an edge consistency-based approach. Specifically, edges in the group-averaged A matrix were only retained if nonzero edge weights were present in at least 60% of participants’ A matrices (96). If not, then edges were set to zero. This process yielded a group-averaged structural connectome with a sparsity value of approximately 8%. This group-averaged structural connectome was used for analyses reported in Figs. 2

to 6. See fig. S12 for sensitivity analyses spanning a range of consistency thresholds and corresponding sparsity values.

Trans-hierarchical state transitions

Cortical hierarchies

Below, we describe three definitions of the cortical hierarchy that were used in the present study to examine trans-hierarchical state transitions.

S-F axis of cytoarchitecture

We primarily characterized the cortical hierarchy using the gradient of cytoarchitectonic similarity developed in previous work (3, 47) and disseminated as part of the BigBrainWarp toolbox (4). Specifically, from BigBrainWarp, we retrieved the histological gradient (“Hist-G2”) corresponding to the S-F axis of cytoarchitecture stored in fsaverage space. Next, we averaged over the vertex values within each of our 200 cortical parcels (see the “Structural connectome construction” section). This process resulted in a 200×1 vector describing the regions’ positions along the S-F axis of cytoarchitectonic similarity.

Alternative hierarchies: T1w/T2w ratio and the gradient of functional connectivity

As stated above and in the main text, our primary constituent of the cortical hierarchy was the S-F axis of cytoarchitectonic similarity. To test the specificity of our primary results, we also examined two other definitions of the cortical hierarchy: the T1w/T2w ratio (23) and the principal gradient of functional connectivity (44).

The T1w/T2w ratio is thought to index cortical microstructure and myelin content in vivo (3, 23). As above, we retrieved this definition of the cortical hierarchy gradient from BigBrainWarp (“Micro-G1”) stored in fsaverage space and averaged over the vertex values within each of our 200 cortical parcels. This process resulted in a 200×1 vector describing the regions’ positions along the MRI proxy of the S-F axis.

The gradient of functional connectivity situates unimodal sensorimotor cortex at one end and transmodal association cortex at the other. Deriving this definition of the cortical hierarchy involves projecting functional connectivity data to a low-dimensional manifold that positions regions with similar functional connectivity profiles near to one another and regions with dissimilar functional connectivity profiles distant from one another. Here, as in our previous work (73), we generated this gradient using whole-brain resting-state functional connectivity obtained from the PNC data (see the “rs-fMRI processing” section). Specifically, for each participant, processed rs-fMRI time series were averaged regionally, and a Pearson correlation coefficient was estimated between each pair of regional time series to generate a functional connectome. Correlation coefficients were normalized using Fisher’s r -to- z transform, and then connectomes were averaged over participants. The principal gradient of functional connectivity was generated from this group-average functional connectome using diffusion map embedding implemented in the BrainSpace toolbox (97). We selected the first gradient output from this approach, which was closely aligned to that observed previously (44). Note that this gradient is the same as that reported in our previous work (73). This process resulted in a 200×1 vector that describes the regions’ positions along the unimodal-to-transmodal (U-T) axis of functional connectivity.

Hierarchical brain states

As discussed in the main text and illustrated in Fig. 1, we divided our 200×1 S-F axis of cytoarchitecture, as well as the T1w/T2w

ratio and U-T axis of functional connectivity, into 20 evenly sized ($n = 10$) and nonoverlapping sets of brain regions that traversed up the cortical hierarchy. This procedure yielded 20 groups of cortical regions that differed on the basis of their position along the cortical hierarchy. Thus, regions within each group had similar profiles of cytoarchitecture, while regions between groups had dissimilar profiles of cytoarchitecture. Moreover, this dissimilarity increased with greater distance between pairs of groups along the S-F axis. These 20 groups of regions formed the brain states that we used in the NCT analysis (see the “Network control theory” section), thus allowing us to model transitions between states moving up and down the cortical hierarchy. See fig. S13 for sensitivity analyses covering different set sizes for brain states.

Network control theory

To model trans-hierarchical state transitions, we used tools from NCT (45, 46, 60, 61). Given an A matrix as input (either group-averaged or individual; see the “Structural connectome construction” section), we first apply the following normalization

$$A = \frac{A}{\lambda(A)_{\max} + c} - I \quad (1)$$

Here, $\lambda(A)_{\max}$ is the largest eigenvalue of A , $c = 1$ to ensure system stability, and I denotes the identity matrix of size $N \times N$. In our analyses, N is equal to the number of brain regions, which is 200. Within this normalized A matrix, we allow each node of the network to carry a real value representing that node’s activity. These values are represented in x and collectively describe the pattern of whole-brain activity as it changes over time. Next, we use a simplified noise-free linear continuous-time and time-invariant model of network dynamics

$$\dot{x} = Ax(t) + B_{\kappa}u_{\kappa}(t) \quad (2)$$

where $x(t)$ is a $N \times 1$ vector that represents the state of the system at time t . The matrix B_{κ} identifies the control input weights, which, by default, we set to the $N \times N$ identity matrix to compute unweighted energy (see the “Minimizing transition energy through optimized control weights” section for the weighted case).

Given the above model of the dynamics (Eq. 2), we compute the control inputs, $u_{\kappa}(t)$, that drive the system from some initial state, x_0 , to some target state, x^* , in a finite amount of time, $T = 1$. Here, initial and target states were constructed using the 20 nonoverlapping groups of 10 brain regions spanning the S-F axis (see the “Hierarchical brain states” section). That is, each initial or target state was defined as an $N \times 1$ vector within which 10 elements that represented cytoarchitecturally similar areas contained a value of 1, and the remaining elements contained a value of 0. Among the many possible inputs, we chose the minimum energy (45) input that minimizes a quadratic cost on the inputs, such that

$$E_{\min} = \min \int_0^T u_{\kappa}^{\top}(t)u_{\kappa}(t)dt \quad (3)$$

subject to Eq. 2. To compute the minimum energy, we construct a useful mathematical object called the controllability Gramian, given by

$$W_c = \int_0^T e^{At}BB^{\top}e^{A^{\top}t}dt \quad (4)$$

where e^{At} is the time-dependent matrix exponential of the matrix A

and is also the impulse response of the system that governs the natural evolution of system dynamics. Then, the minimum energy is given by

$$E_{\min} = (e^{A^t}x_0 - x^*)^T W_c^{-1}(e^{A^t}x_0 - x^*) \quad (5)$$

Intuitively, the quantity in the parentheses measures the difference between the natural evolution of the system from the initial condition, $e^{A^t}x_0$, and the target state, x^* . This difference is precisely the difference for which the control input $u_k(t)$ needs to compensate, and the projection of this difference onto W_c^{-1} yields the minimum energy for providing such compensation (46).

Transition energy and energy asymmetries

We used the above derivation of minimum control energy to compute a $k \times k$ transition energy matrix, T_E . Elements of T_E quantified the minimum energy (E) required to transition between all possible pairs of $k = 20$ brain states, where brain states were based on the subsets of regions sampled along the S-F axis of cytoarchitecture outlined above (see the "Cortical hierarchies" section). Following from the above equations, we interpret transition energy as the amount of effort the control signals had to exert to compensate for the difference between the natural (i.e., uncontrolled) and the desired (i.e., controlled) evolutions of the system. In this way, lower transition energy corresponds to less need for control input, which, in turn, confers a transition that is easier for the model to complete. Thus, we interpret differences in transition energy as differences in the ease with which dynamics can be controlled to propagate across the S-F axis of cytoarchitecture.

As mentioned in the main text and above, the hierarchically ordered nature of our brain states endowed T_E with a distinction between transitions moving up the hierarchy (bottom-up energy) and those moving down the hierarchy (top-down energy). Furthermore, these bottom-up and top-down transition energies were naturally compartmentalized into the upper and lower triangles of T_E , respectively. Hence, asymmetries between bottom-up and top-down energy for all state pairs were calculated as $T_{E\Delta} = T_E - T_E^T$. Note that, unlike T_E , $T_{E\Delta}$ is symmetrical; thus, only the upper triangle was carried forward for asymmetry analysis.

Bootstrap test for energy asymmetries

In Fig. 2, we showed that bottom-up energy was lower than top-down (negative mean $T_{E\Delta}$) and that $T_{E\Delta}$ was negatively correlated with the distance that separated states along the hierarchy. To examine whether these effects were robust to sampling variability, we calculated $T_{E\Delta}$ in each of 1000 bootstrapped versions of our group-averaged structural connectome. Specifically, we reproduced our group-averaged structural connectome for each of 1000 bootstrapped samples comprising 50% of our 793 participant connectomes ($n = 396$). Then, we reestimated $T_{E\Delta}$ in each of these 1000 bootstrapped connectomes. This procedure allowed us to estimate 95% CIs on the mean $T_{E\Delta}$ and the correlation with hierarchical distance (see Fig. 2, A and B).

Null network models

In addition to our above bootstrap test, we compared both the mean $T_{E\Delta}$ and the correlation with hierarchical distance to null distributions generated using two different spatially embedded null network models (49). Alongside preserving the spatial embedding of network nodes, these null network models randomly rewired the network while preserving either the edge distribution or the strength distribution of the network. For each of these null

models, we produced 10,000 rewired networks derived from the group-averaged structural connectome (see the "Structural connectome construction" section). Then, to generate empirical null distributions, upon each rewired network, we recomputed $T_{E\Delta}$ and the corresponding hierarchy distance correlation. Lastly, P values were estimated as the probability that the magnitude of the observed values occurred under a given null.

Comparison with measures of communicability

As mentioned in the main text, we compared our energy asymmetries ($T_{E\Delta}$) to asymmetric measures of network communicability taken from past literature, namely, diffusion efficiency (de), search information (si), and a modified version of path transitivity (pt). We implemented de and si following past literature; as such, we refer readers to (43, 50–52) and the Brain Connectivity Toolbox (<https://sites.google.com/site/bctnet/>; `diffusion_efficiency.m` and `search_information.m`) for details. For path transitivity, we developed a modified version that incorporated asymmetries by examining the cumulative pt over successively longer segments of the shortest path. Below, we describe the original definition of path transitivity before describing our modification.

Path transitivity is sensitive to the number of local detours (i.e., those that traverse only two edges) that are present along the shortest path connecting two nodes: source and target. To estimate path transitivity, the matching index between all possible pairs of nodes is first estimated as follows

$$m_{ij} = \frac{\sum : k \neq i, j (w_{ik} + w_{jk}) \Theta(w_{ik}) \Theta(w_{jk})}{\sum : k \neq j w_{ik} + \sum : k \neq i w_{jk}} \quad (6)$$

where w_{ij} is the weight of the edge between nodes i and j , and k denotes the node along a detour between nodes i and j . The quantity $\Theta(w_{ik}) = 1$ if $w_{ik} > 0$ and 0 otherwise, and the quantity $\Theta(w_{jk}) = 1$ if $w_{jk} > 0$ and 0 otherwise. Then, assuming a sequence of nodes, $\Omega_{s \rightarrow t} = \{s, a, b, c, d, t\}$, that comprise a shortest path, path transitivity is calculated by summing the matching index for each pair of nodes as follows

$$pt(\Omega_{s \rightarrow t}) = \frac{2 \sum_{i \in \Omega} \sum_{j \in \Omega} m_{ij}}{|\Omega_{s \rightarrow t}| (|\Omega_{s \rightarrow t}| - 1)} \quad (7)$$

where $|\Omega_{s \rightarrow t}|$ denotes the number of nodes in $\Omega_{s \rightarrow t}$, and hence, $|\Omega_{s \rightarrow t}| (|\Omega_{s \rightarrow t}| - 1)$ is the total number of pairs of nodes comprising $\Omega_{s \rightarrow t}$. Because A is weighted in our study, a higher pt confers a path with higher strength of local returning detours.

To endow path transitivity with asymmetry, we performed the following modification. We calculated pt separately for each segment of $\Omega_{s \rightarrow t}$ that began at the source node (Fig. 3B): $\Omega_{s \rightarrow a} = \{s, a\}$, $\Omega_{s \rightarrow b} = \{s, a, b\}$, $\Omega_{s \rightarrow c} = \{s, a, b, c\}$, $\Omega_{s \rightarrow d} = \{s, a, b, c, d\}$, and $\Omega_{s \rightarrow t} = \{s, a, b, c, d, t\}$. Critically, for each of these segments, the denominator in Eq. 7 remained fixed as $|\Omega_{s \rightarrow t}| (|\Omega_{s \rightarrow t}| - 1)$. This choice resulted in the pt of each segment being normalized by the full shortest path, which guaranteed that the transitivity of each segment approached the transitivity of the full shortest path. The pt of each segment was assembled as $n \times 1$ vector, pt_c , where n is the number of segments, which, in turn, is equal to the length of the shortest path. We refer to this vector as cumulative path transitivity. Next, we reestimated cumulative path transitivity for segments starting from the target node, thus obtaining pt_c for both directions along the shortest path, $pt_{c, s \rightarrow t}$ and $pt_{c, t \rightarrow s}$ (Fig. 3C).

Lastly, we subtracted these vectors elementwise and summed the differences, $pt_{c\Delta} = \sum (pt_{c, s \rightarrow t} - pt_{c, t \rightarrow s})$. A positive $pt_{c\Delta}$ states that path transitivity accumulated more quickly when traversing from source to target compared to target to source. Intuitively, this means that high-strength local detours were encountered sooner while traversing from source to target compared to the reverse. Thus, $pt_{c\Delta}$ is asymmetric.

Uncontrolled dynamics

In addition to examining the energy required to complete state transitions between specific state pairs, we also examined how uncontrolled dynamics spread naturally across the cortex from each of our cytoarchitectonic brain states. Specifically, for each brain state, we set the constituent regions' activity to 1 and all other regions' activity to 0. Then, we allowed the activity to diffuse in an uncontrolled manner along the networks' edges over time according to $\dot{x} = Ax(t)$. This approach stands in contrast to the approach that we have discussed thus far of guiding activity to flow from one state to another via a set of control signals. As mentioned in the main text, for each seed brain state and time point t , we correlated the pattern of simulated activity at each node with the S-F axis of cytoarchitecture. Results of this analysis are shown in Fig. 4 (B and C).

Intrinsic neuronal time scales

As mentioned in the main text, we sought to validate our transition energy analysis in functional data using intrinsic neuronal time scales derived from ECoG data. Thus, we compared energy asymmetries from our NCT analysis with differences between brain states' intrinsic time scales. Following previous work (24), we estimated the regions' intrinsic time scales using the time constant, τ , of an exponential decay function fitted to the autocorrelation function of ECoG time series. Specifically, we downloaded sensor-level τ data processed by Gao *et al.* (24) (https://github.com/rdgao/field-echos/blob/master/data/df_human.csv) and, using the provided Montreal Neurological Institute (MNI) coordinates, matched each sensor to our parcellation (200 Schaefer parcels); matching was done by finding the smallest Euclidean distance between each sensor and the centroid of each parcel. We then averaged τ over sensors within each parcel and over regions within each cytoarchitectonic brain state. This process generated state-level τ values that were then subtracted to produce τ_{Δ} , a matrix of change in τ between all pairs of brain states.

Effective connectivity

As mentioned in the main text, we sought to validate our transition energy analysis in functional data using EC derived from rs-fMRI data. Thus, we compared energy asymmetries from our NCT analysis with asymmetries in EC. EC was estimated using spDCM (57) implemented in SPM12 r7765 (Wellcome Trust Centre for Neuroimaging, London, UK). To generate time series for modeling effective connectivity, we first averaged participants' processed rs-fMRI data across the regions that comprised each cytoarchitectonic brain state. This process yielded one time series of 120 volumes per subject per brain state. Next, owing to the low number of volumes in our rs-fMRI acquisition, we deployed an averaging and concatenation approach that yielded a single group-averaged time series of 1200 volumes for each brain state. This process proceeded as follows. First, we randomly excluded 3 participants from our

sample to retain 790 participants. Second, we divided our sample of 790 participants into 10 equally sized groups ($n = 79$) and averaged the state-level rs-fMRI time series across participants within each group separately. Last, we concatenated these group-averaged time series end-to-end across the 10 groups. This process yielded resting-state time series for each brain state with 1200 volumes that represented averages over distinct subsets of participants taken from our sample. These time series were used as inputs to the spDCM algorithm, together with a fully connected model of coupling strengths, enabling the estimation of EC between all cytoarchitectonic brain states spanning the S-F axis. As per our primary analysis of transition energies, EC estimates were trivially grouped into bottom-up and top-down and were then subtracted to create an EC asymmetry matrix.

Minimizing transition energy through optimized control weights

Our primary analyses involved examining uniformly weighted transition energies, where all nodes of the dynamical system were assigned control weights equal to 1 (i.e., setting the diagonal entries of B_k in Eq. 2 to the $N \times N$ identity matrix). This uniform weighting meant that all brain regions were endowed with the same degree of control over all $k \times k$ state transitions. However, as discussed in the main text (see the "Optimized control weights track the S-F axis of cytoarchitecture and increase energy asymmetries" section), we were also interested in examining regional variation in facilitating trans-hierarchical state transitions.

To achieve this goal, we systematically perturbed each region's degree of control over the system and measured the corresponding change in transition energies. Specifically, for each brain region, i , we recomputed T_E after adding a constant amount of additional control to the corresponding diagonal element of B_k (the remaining diagonal entries were left equal to 1). This process generated a $k \times k \times 200$ matrix of perturbed transition energies, P_E . Next, for each perturbed region (dimension 3 of P_E), we subtracted the perturbed transition energies from the uniformly weighted energies (T_E) to create $P_{E\Delta}$, a $k \times k \times 200$ matrix of perturbed transition energy delta values. For each state transition, this subtraction yielded a 200×1 vector that quantified how perturbing each node of the system one at a time—by a constant arbitrary amount—affected transition energy. Note that increasing the influence of a single node's control necessarily reduces energy; the task of completing a state transition is easier for the model when any node in B_k is granted a greater degree of control over the system, leading to lower energy. Accordingly, all values in $P_{E\Delta}$ were positive, and the magnitude of these deltas encoded the relative importance of each region to completing a specific state transition, with regions with larger deltas being more important.

To assess correspondence with the S-F axis, we calculated the Spearman rank correlation between perturbed deltas for each state transition and the S-F axis. The spatial embedding of perturbed delta values varied as a function of the location of the initial and target states on the S-F axis. To account for this, instead of correlating deltas with the S-F axis directly, we correlated them with the distance separating nodes from the initial and target state separately and retained the strongest correlation coefficient. In this way, any observed correlation captures the extent to which deltas vary as a function of hierarchical distance from the states that comprise a given transition. Note that nodes that were within

the initial and target states were excluded when calculating correlations. Thus, coupling between the delta values and the S-F axis was only assessed in the remaining bystander regions. We assigned P values using BrainSMASH (<https://brainsmash.readthedocs.io/>) (58) and corrected for multiple comparisons via the Benjamini and Hochberg FDR ($q = 0.05$) procedure (59). The spatial autocorrelation embedded in neuroimaging data can lead to inflated P values in spatial correlation analyses and must be accounted for in the creation of null models. BrainSMASH addresses this by generating null brain maps that match the spatial autocorrelation properties of the input data. We used BrainSMASH to generate 10,000 spatial autocorrelation-preserving null maps of the S-F axis, generating a null distribution of Spearman rank correlations.

We reestimated T_E (and $T_{E\Delta}$) one more time using each state transition's vector of perturbed deltas as optimized control weights. This process yielded optimized trans-hierarchical transition energies and energy asymmetries. Lastly, to assess whether the size of the mean $T_{E\Delta}$ was significantly different for optimized weights compared to uniform weights, we derived $T_{E\Delta}$ for both weight sets using bootstrapped group-averaged connectomes (see the "Bootstrap test for energy asymmetries" section) and assigned 95% CIs to the mean $T_{E\Delta}$.

Age effects

As mentioned in the main text, we sought to link participant-specific energy asymmetries with age to examine developmental effects. To achieve this goal, we derived T_E and $T_{E\Delta}$ from each participant's A matrix (see the "Structural connectome construction" section) using optimized control weights. Note that the process of computing optimized transition energies was performed on a subject-specific basis using subject-specific optimized control weights; this was done by applying the above perturbation procedure (see the "Minimizing transition energy through optimized control weights" section) to each participant's A matrix separately (see fig. S14 for correlations between participant-specific optimized weights and the gradient of cytoarchitecture). Next, for each state transition, we calculated the Pearson's correlation between T_E and age while controlling for sex, total brain volume, edge density, and in-scanner motion (see the "Imaging-derived nuisance covariates" section). We repeated this process for energy asymmetries averaged over bottom-up and top-down energy, where energy was averaged over the upper and lower triangles of each participant's T_E matrix, respectively, before being subtracted.

In addition to estimating within-sample age effects, we also sought to test whether energy asymmetries could be used to predict the participants' ages in out-of-sample testing. To achieve this, we assembled the upper triangle of each subject's $T_{E\Delta}$ matrix into a 793×190 feature table, X . Then, we used a cross-validated ridge regression model implemented in scikit-learn (98) with default parameters ($\alpha = 1$) to predict participants' ages (y). Specifically, we assessed out-of-sample prediction performance using 10-fold cross-validation scored by root mean squared error (RMSE), mean absolute error (MAE), and the correlation between the true y and predicted y . As per scikit-learn defaults, to standardize the interpretation of all scoring metrics as higher scores represent better performance, we flipped the sign for RMSE and MAE.

Models were trained using all columns of X as input features, and scoring metrics were each averaged across folds. As above, we included sex, total brain volume, edge density, and in-scanner

motion as nuisance covariates. Nuisance covariates were controlled for by regressing their effect out of X before predicting y . Within each fold, nuisance covariates were fit to the training data and applied to the test data to prevent leakage. Subsequently, we applied principal components (PCs) analysis to reduce the dimensionality of X , retaining enough PCs to explain 80% of the variance in the data. Lastly, owing to evidence that prediction performance can be biased by the arbitrariness of a single split of the data (99), we repeated 10-fold cross-validation 100 times, each time with a different random 10-fold split. This process yielded a distribution of 100 mean negative RMSE values, 100 mean negative MAE values, and 100 mean correlations between true y and predicted y .

Our above prediction model generated robust estimates of prediction performance, but it did not examine whether prediction performance was itself significant. To test whether the prediction performance was better than chance, we compared point estimates of each of our scoring metrics—taken as the mean over the 100 values—to the distribution of values obtained from permuted data. Specifically, we subjected the point estimates of our scoring metrics to 10,000 random permutations, wherein the rows (i.e., participants) of y were randomly shuffled.

Citation diversity statement

Recent work in several fields of science has identified a bias in citation practices such that papers from women and other minority scholars are undercited relative to the number of such papers in the field (100–108). Here, we sought to proactively consider choosing references that reflect the diversity of the field in thought, form of contribution, gender, race, ethnicity, and other factors. First, we obtained the predicted gender of the first and last author of each reference by using databases that store the probability of a first name being carried by a woman (104, 109). By this measure (and excluding self-citations to the first and last authors of our current paper), our references contain 5.25% woman (first)/woman (last), 10.54% man/woman, 14.73% woman/man, and 69.48% man/man. This method is limited in that (i) names, pronouns, and social media profiles used to construct the databases may not, in every case, be indicative of gender identity, and (ii) it cannot account for intersex, nonbinary, or transgendered people. Second, we obtained the predicted racial/ethnic category of the first and last author of each reference by databases that store the probability of a first and last name being carried by an author of color (110, 111). By this measure (and excluding self-citations), our references contain 6.17% author of color (first)/author of color (last), 16.91% white author/author of color, 24.19% author of color/white author, and 52.73% white author/white author. This method is limited in that (i) names and Florida Voter Data to make the predictions may not be indicative of racial/ethnic identity, and (ii) it cannot account for Indigenous and mixed-race authors or those who may face differential biases due to the ambiguous racialization or ethnicization of their names. We look forward to future work that could help us to better understand how to support equitable practices in science.

Supplementary Materials

This PDF file includes:

Figs. S1 to S14

[View/request a protocol for this paper from Bio-protocol.](#)

REFERENCES AND NOTES

- M. Á. García-Cabezas, B. Zikopoulos, H. Barbas, The structural model: A theory linking connections, plasticity, pathology, development and evolution of the cerebral cortex. *Brain Struct. Funct.* **224**, 985–1008 (2019).
- M. Á. García-Cabezas, J. L. Hacker, B. Zikopoulos, A protocol for cortical type analysis of the human neocortex applied on histological samples, the atlas of Von Economo and Koskinas, and magnetic resonance imaging. *Front. Neuroanat.* **14**, 576015 (2020).
- C. Paquola, R. Vos De Wael, K. Wagstyl, R. A. I. Bethlehem, S.-J. Hong, J. Seidlitz, E. T. Bullmore, A. C. Evans, B. Misic, D. S. Margulies, J. Smallwood, B. C. Bernhardt, Microstructural and functional gradients are increasingly dissociated in transmodal cortices. *PLOS Biol.* **17**, e3000284 (2019).
- C. Paquola, J. Royer, L. B. Lewis, C. Lepage, T. Glatard, K. Wagstyl, J. DeKraker, P.-J. Toussaint, S. L. Valk, D. L. Collins, A. Khan, K. Amunts, A. C. Evans, T. Dickscheid, B. C. Bernhardt, The BigBrainWarp toolbox for integration of BigBrain 3D histology with multimodal neuroimaging. *eLife* **10**, e70119 (2021).
- V. J. Sydnor, B. Larsen, D. S. Bassett, A. Alexander-Bloch, D. A. Fair, C. Liston, A. P. Mackey, M. P. Milham, A. Pines, D. R. Roalf, J. Seidlitz, T. Xu, A. Raznahan, T. D. Satterthwaite, Neurodevelopment of the association cortices: Patterns, mechanisms, and implications for psychopathology. *Neuron* **109**, 2820–2846 (2021).
- M. Mesulam, From sensation to cognition. *Brain* **121**, 1013–1052 (1998).
- M. Mesulam, Representation, inference, and transcendent encoding in neurocognitive networks of the human brain. *Ann. Neurol.* **64**, 367–378 (2008).
- B. Vázquez-Rodríguez, Z.-Q. Liu, P. Hagmann, B. Misic, Signal propagation via cortical hierarchies. *Netw. Neurosci.* **4**, 1072–1090 (2020).
- D. J. Felleman, D. C. Van Essen, Distributed hierarchical processing in the primate cerebral cortex. *Cereb. Cortex* **1**, 1–47 (1991).
- K. S. Rockland, D. N. Pandya, Laminar origins and terminations of cortical connections of the occipital lobe in the rhesus monkey. *Brain Res.* **179**, 3–20 (1979).
- J. A. Harris, S. Mihalas, K. E. Hirokawa, J. D. Whitesell, H. Choi, A. Bernard, P. Bohn, S. Caldejon, L. Casal, A. Cho, A. Feiner, D. Feng, N. Gaudreault, C. R. Gerfen, N. Graddis, P. A. Groblewski, A. M. Henry, A. Ho, R. Howard, J. E. Knox, L. Kuan, X. Kuang, J. Lecoq, P. Lesnar, Y. Li, J. Luviano, S. McConoughey, M. T. Mortrud, M. Naemi, L. Ng, S. W. Oh, B. Ouellette, E. Shen, S. A. Sorensen, W. Wakeman, Q. Wang, Y. Wang, A. Williford, J. W. Phillips, A. R. Jones, C. Koch, H. Zeng, Hierarchical organization of cortical and thalamic connectivity. *Nature* **575**, 195–202 (2019).
- K. Rauss, G. Pourtois, What is bottom-up and what is top-down in predictive coding? *Front. Psychol.* **4**, 276 (2013).
- J. Vezoli, L. Magrou, R. Goebel, X.-J. Wang, K. Knoblauch, M. Vinck, H. Kennedy, Cortical hierarchy, dual counterstream architecture and the importance of top-down generative networks. *Neuroimage* **225**, 117479 (2021).
- Y. Zhou, K. J. Friston, P. Zeidman, J. Chen, S. Li, A. Razi, The hierarchical organization of the default, dorsal attention and salience networks in adolescents and young adults. *Cereb. Cortex* **28**, 726–737 (2018).
- S. J. Kiebel, J. Daunizeau, K. J. Friston, A hierarchy of time-scales and the brain. *PLoS Comput. Biol.* **4**, e1000209 (2008).
- K. Friston, The free-energy principle: A unified brain theory? *Nat. Rev. Neurosci.* **11**, 127–138 (2010).
- G. Pezzulo, M. Levin, Top-down models in biology: Explanation and control of complex living systems above the molecular level. *J. R. Soc. Interface* **13**, 20160555 (2016).
- H. Barbas, M. Á. García-Cabezas, How the prefrontal executive got its stripes. *Curr. Opin. Neurobiol.* **40**, 125–134 (2016).
- S. N. Haber, H. Liu, J. Seidlitz, E. Bullmore, Prefrontal connectomics: From anatomy to human imaging. *Neuropsychopharmacology* **47**, 20–40 (2022).
- H. Barbas, General cortical and special prefrontal connections: Principles from structure to function. *Annu. Rev. Neurosci.* **38**, 269–289 (2015).
- N. T. Markov, J. Vezoli, P. Chameau, A. Falchier, R. Quilodran, C. Huissoud, C. Lamy, P. Misery, P. Giroud, S. Ullman, P. Barone, C. Dehay, K. Knoblauch, H. Kennedy, Anatomy of hierarchy: Feedforward and feedback pathways in macaque visual cortex. *J. Comp. Neurol.* **522**, 225–259 (2014).
- S. F. Beul, C. C. Hilgetag, Towards a “canonical” agranular cortical microcircuit. *Front. Neuroanat.* **8**, 165 (2015).
- M. F. Glasser, D. C. Van Essen, Mapping human cortical areas in vivo based on myelin content as revealed by T1- and T2-weighted MRI. *J. Neurosci.* **31**, 11597–11616 (2011).
- R. Gao, R. L. van den Brink, T. Pfeffer, B. Voytek, Neuronal timescales are functionally dynamic and shaped by cortical microarchitecture. *eLife* **9**, e61277 (2020).
- Y. Wei, L. H. Scholtens, E. Turk, M. P. van den Heuvel, Multiscale examination of cytoarchitectonic similarity and human brain connectivity. *Netw. Neurosci.* **3**, 124–137 (2019).
- C. R. Cadwell, A. Bhaduri, M. A. Mostajo-Radji, M. G. Keefe, T. J. Nowakowski, Development and arealization of the cerebral cortex. *Neuron* **103**, 980–1004 (2019).
- A. Kriegstein, S. Noctor, V. Martínez-Cerdeño, Patterns of neural stem and progenitor cell division may underlie evolutionary cortical expansion. *Nat. Rev. Neurosci.* **7**, 883–890 (2006).
- E. Lewitus, I. Kelava, W. B. Huttner, Conical expansion of the outer subventricular zone and the role of neocortical folding in evolution and development. *Front. Hum. Neurosci.* **7**, 424 (2013).
- A. Pontious, T. Kowalczyk, C. Englund, R. F. Hevner, Role of intermediate progenitor cells in cerebral cortex development. *Dev. Neurosci.* **30**, 24–32 (2008).
- J. van den Amele, L. Tiberi, P. Vanderhaeghen, I. Espuny-Camacho, Thinking out of the dish: What to learn about cortical development using pluripotent stem cells. *Trends Neurosci.* **37**, 334–342 (2014).
- P. Rakic, Neurogenesis in adult primate neocortex: An evaluation of the evidence. *Nat. Rev. Neurosci.* **3**, 65–71 (2002).
- P. R. Huttenlocher, C. de Courten, L. J. Garey, H. Van der Loos, Synaptogenesis in human visual cortex—Evidence for synapse elimination during normal development. *Neurosci. Lett.* **33**, 247–252 (1982).
- P. R. Huttenlocher, Synaptic density in human frontal cortex—Developmental changes and effects of aging. *Brain Res.* **163**, 195–205 (1979).
- B. D. Semple, K. Blomgren, K. Gimlin, D. M. Ferriero, L. J. Noble-Haeusslein, Brain development in rodents and humans: Identifying benchmarks of maturation and vulnerability to injury across species. *Prog. Neurobiol.* **106–107**, 1–16 (2013).
- G. L. Baum, R. Ciric, D. R. Roalf, R. F. Betzel, T. M. Moore, R. T. Shinohara, A. E. Kahn, S. N. Vandeekar, P. E. Rupert, M. Quarmley, P. A. Cook, M. A. Elliott, K. Ruparel, R. E. Gur, R. C. Gur, D. S. Bassett, T. D. Satterthwaite, Modular segregation of structural brain networks supports the development of executive function in youth. *Curr. Biol.* **27**, 1561–1572.e8 (2017).
- R. L. Buckner, F. M. Krienen, The evolution of distributed association networks in the human brain. *Trends Cogn. Sci.* **17**, 648–665 (2013).
- J. Hill, T. Inder, J. Neil, D. Dierker, J. Harwell, D. Van Essen, Similar patterns of cortical expansion during human development and evolution. *Proc. Natl. Acad. Sci. U.S.A.* **107**, 13135–13140 (2010).
- R. K. Lenroot, J. N. Giedd, Brain development in children and adolescents: Insights from anatomical magnetic resonance imaging. *Neurosci. Biobehav. Rev.* **30**, 718–729 (2006).
- K. L. Mills, A.-L. Goddings, M. M. Herting, R. Meuwese, S.-J. Blakemore, E. A. Crone, R. E. Dahl, B. Güroğlu, A. Raznahan, E. R. Sowell, C. K. Tamnes, Structural brain development between childhood and adulthood: Convergence across four longitudinal samples. *Neuroimage* **141**, 273–281 (2016).
- C. K. Tamnes, Y. Østby, A. M. Fjell, L. T. Westlye, P. Due-Tønnessen, K. B. Walhovd, Brain maturation in adolescence and young adulthood: Regional age-related changes in cortical thickness and white matter volume and microstructure. *Cereb. Cortex* **20**, 534–548 (2010).
- C. K. Tamnes, M. M. Herting, A.-L. Goddings, R. Meuwese, S.-J. Blakemore, R. E. Dahl, B. Güroğlu, A. Raznahan, E. R. Sowell, E. A. Crone, K. L. Mills, Development of the cerebral cortex across adolescence: A multisample study of inter-related longitudinal changes in cortical volume, surface area, and thickness. *J. Neurosci.* **37**, 3402–3412 (2017).
- B. Mišić, R. F. Betzel, A. Nematzadeh, J. Goñi, A. Griffa, P. Hagmann, A. Flammini, Y.-Y. Ahn, O. Sporns, Cooperative and competitive spreading dynamics on the human connectome. *Neuron* **86**, 1518–1529 (2015).
- C. Seguin, A. Razi, A. Zalesky, Inferring neural signalling directionality from undirected structural connectomes. *Nat. Commun.* **10**, 4289 (2019).
- D. S. Margulies, S. S. Ghosh, A. Goulas, M. Falkiewicz, J. M. Huntenburg, G. Langs, G. Bezgin, S. B. Eickhoff, F. X. Castellanos, M. Petrides, E. Jefferies, J. Smallwood, Situating the default-mode network along a principal gradient of macroscale cortical organization. *Proc. Natl. Acad. Sci. U.S.A.* **113**, 12574–12579 (2016).
- T. M. Karrer, J. Z. Kim, J. Stiso, A. E. Kahn, F. Pasqualetti, U. Habel, D. S. Bassett, A practical guide to methodological considerations in the controllability of structural brain networks. *J. Neural Eng.* **17**, 026031 (2020).
- J. Z. Kim, D. S. Bassett, Linear dynamics & control of brain networks. arXiv:1902.03309 [physics, q-bio] (2019).
- C. Paquola, J. Seidlitz, O. Benkarim, J. Royer, P. Klimes, R. A. I. Bethlehem, S. Larivière, R. Vos de Wael, R. Rodríguez-Cruces, J. A. Hall, B. Fauscher, J. Smallwood, B. C. Bernhardt, A multi-scale cortical wiring space links cellular architecture and functional dynamics in the human brain. *PLoS Biol.* **18**, e3000979 (2020).
- T. D. Satterthwaite, J. J. Connolly, K. Ruparel, M. E. Calkins, C. Jackson, M. A. Elliott, D. R. Roalf, R. Hopson, K. Prabhakaran, M. Behr, H. Qiu, F. D. Mentch, R. Chiavacci, P. M. A. Sleiman, R. C. Gur, H. Hakonarson, R. E. Gur, The Philadelphia neurodevelopmental

- cohort: A publicly available resource for the study of normal and abnormal brain development in youth. *Neuroimage* **124**, 1115–1119 (2016).
49. J. A. Roberts, A. Perry, A. R. Lord, G. Roberts, P. B. Mitchell, R. E. Smith, F. Calamante, M. Breakspear, The contribution of geometry to the human connectome. *Neuroimage* **124**, 379–393 (2016).
 50. J. Goñi, A. Avena-Koenigsberger, N. Velez de Mendizabal, M. P. van den Heuvel, R. F. Betzel, O. Sporns, Exploring the morphospace of communication efficiency in complex networks. *PLOS ONE* **8**, e58070 (2013).
 51. M. Rosvall, A. Grönlund, P. Minnhagen, K. Sneppen, Searchability of networks. *Phys. Rev. E* **72**, 046117 (2005).
 52. J. Goñi, M. P. van den Heuvel, A. Avena-Koenigsberger, N. Velez de Mendizabal, R. F. Betzel, A. Griffa, P. Hagmann, B. Corominas-Murtra, J.-P. Thiran, O. Sporns, Resting-brain functional connectivity predicted by analytic measures of network communication. *Proc. Natl. Acad. Sci. U.S.A.* **111**, 833–838 (2014).
 53. S. L. Valk, T. Xu, C. Paquola, B. Park, R. A. I. Bethlehem, R. Vos de Wael, J. Royer, S. K. Masouleh, Ş. Bayrak, P. Kochunov, B. T. T. Yeo, D. Margulies, J. Smallwood, S. B. Eickhoff, B. C. Bernhardt, Genetic and phylogenetic uncoupling of structure and function in human transmodal cortex. *Nat. Commun.* **13**, 2341 (2022).
 54. G. L. Baum, Z. Cui, D. R. Roalf, R. Ciric, R. F. Betzel, B. Larsen, M. Cieslak, P. A. Cook, C. H. Xia, T. M. Moore, K. Ruparel, D. J. Oathes, A. F. Alexander-Bloch, R. T. Shinohara, A. Raznahan, R. E. Gur, R. C. Gur, D. S. Bassett, T. D. Satterthwaite, Development of structure–function coupling in human brain networks during youth. *Proc. Natl. Acad. Sci. U.S.A.* **117**, 771–778 (2020).
 55. B. Vázquez-Rodríguez, L. E. Suárez, R. D. Markello, G. Shafiei, C. Paquola, P. Hagmann, M. P. van den Heuvel, B. C. Bernhardt, R. N. Spreng, B. Misic, Gradients of structure–function tethering across neocortex. *Proc. Natl. Acad. Sci. U.S.A.* **116**, 21219–21227 (2019).
 56. B. Frauscher, N. von Ellenrieder, R. Zelmann, I. Doležalová, L. Minotti, A. Olivier, J. Hall, D. Hoffmann, D. K. Nguyen, P. Kahane, F. Dubeau, J. Gotman, Atlas of the normal intracranial electroencephalogram: Neurophysiological awake activity in different cortical areas. *Brain* **141**, 1130–1144 (2018).
 57. K. J. Friston, J. Kahan, B. Biswal, A. Razi, A DCM for resting state fMRI. *Neuroimage* **94**, 396–407 (2014).
 58. J. B. Burt, M. Helmer, M. Shinn, A. Anticevic, J. D. Murray, Generative modeling of brain maps with spatial autocorrelation. *Neuroimage* **220**, 117038 (2020).
 59. Y. Benjamini, Y. Hochberg, Controlling the false discovery rate: A practical and powerful approach to multiple testing. *J. R. Stat. Soc. B. Methodol.* **57**, 289–300 (1995).
 60. T. Menara, V. Katewa, D. S. Bassett, F. Pasqualetti, The structured controllability radius of symmetric (brain) networks, in *2018 Annual American Control Conference (ACC)* (IEEE, Milwaukee, WI, 2018), pp. 2802–2807.
 61. F. Pasqualetti, S. Zampieri, F. Bullo, Controllability metrics, limitations and algorithms for complex networks. *IEEE Trans. Control Netw. Syst.* **1**, 40–52 (2014).
 62. A. Goulas, K. Zilles, C. C. Hilgetag, Cortical gradients and laminar projections in mammals. *Trends Neurosci.* **41**, 775–788 (2018).
 63. A. Goulas, R. Werner, S. F. Beul, D. Säring, M. van den Heuvel, L. C. Triarhou, C. C. Hilgetag, Cytoarchitectonic similarity is a wiring principle of the human connectome. *bioRxiv*, 068254 (2016).
 64. A. Avena-Koenigsberger, X. Yan, A. Kolchinsky, M. P. van den Heuvel, P. Hagmann, O. Sporns, A spectrum of routing strategies for brain networks. *PLoS Comput. Biol.* **15**, e1006833 (2019).
 65. D. Zhou, C. W. Lynn, Z. Cui, R. Ciric, G. L. Baum, T. M. Moore, D. R. Roalf, J. A. Detre, R. C. Gur, R. E. Gur, T. D. Satterthwaite, D. S. Bassett, Efficient coding in the economics of human brain connectomics. *Netw. Neurosci.* **6**, 234–274 (2022).
 66. H. Ju, J. Z. Kim, J. M. Beggs, D. S. Bassett, Network structure of cascading neural systems predicts stimulus propagation and recovery. *J. Neural Eng.* **17**, 056045 (2020).
 67. L. Chanes, L. F. Barrett, Redefining the role of limbic areas in cortical processing. *Trends Cogn. Sci.* **20**, 96–106 (2016).
 68. A. Wolff, N. Berberian, M. Golesorkhi, J. Gomez-Pilar, F. Zilio, G. Northoff, Intrinsic neural timescales: Temporal integration and segregation. *Trends Cogn. Sci.* **26**, 159–173 (2022).
 69. S. T. E. Baker, D. I. Lubman, M. Yucel, N. B. Allen, S. Whittle, B. D. Fulcher, A. Zalesky, A. Fornito, Developmental changes in brain network hub connectivity in late adolescence. *J. Neurosci.* **35**, 9078–9087 (2015).
 70. M. Kaiser, Mechanisms of connectome development. *Trends Cogn. Sci.* **21**, 703–717 (2017).
 71. S. Oldham, A. Fornito, The development of brain network hubs. *Dev. Cogn. Neurosci.* **36**, 100607 (2019).
 72. Z. Cui, J. Stiso, G. L. Baum, J. Z. Kim, D. R. Roalf, R. F. Betzel, S. Gu, Z. Lu, C. H. Xia, X. He, R. Ciric, D. J. Oathes, T. M. Moore, R. T. Shinohara, K. Ruparel, C. Davatzikos, F. Pasqualetti, R. E. Gur, R. C. Gur, D. S. Bassett, T. D. Satterthwaite, Optimization of energy state transition trajectory supports the development of executive function during youth. *eLife* **9**, e53060 (2020).
 73. L. Parkes, T. M. Moore, M. E. Calkins, M. Cieslak, D. R. Roalf, D. H. Wolf, R. C. Gur, R. E. Gur, T. D. Satterthwaite, D. S. Bassett, Network controllability in transmodal cortex predicts psychosis spectrum symptoms. *Biol. Psychiatry* **89**, S370–S371 (2021).
 74. E. J. Cornblath, A. Ashourvan, J. Z. Kim, R. F. Betzel, R. Ciric, A. Adebimpe, G. L. Baum, X. He, K. Ruparel, T. M. Moore, R. C. Gur, R. E. Gur, R. T. Shinohara, D. R. Roalf, T. D. Satterthwaite, D. S. Bassett, Temporal sequences of brain activity at rest are constrained by white matter structure and modulated by cognitive demands. *Commun. Biol.* **3**, 261 (2020).
 75. E. Nozari, J. Stiso, L. Caciagli, E. J. Cornblath, X. He, M. A. Bertolero, A. S. Mahadevan, G. J. Pappas, D. S. Bassett, Is the brain macroscopically linear? A system identification of resting state dynamics. arXiv:2012.12351 [cs, eess, math, q-bio] (2020).
 76. L. Riedel, M. P. van den Heuvel, S. Markett, Trajectory of rich club properties in structural brain networks. *Hum. Brain Mapp.* **43**, 4239–4253 (2022).
 77. A. F. G. Rosen, D. R. Roalf, K. Ruparel, J. Blake, K. Seelaus, L. P. Villa, R. Ciric, P. A. Cook, C. Davatzikos, M. A. Elliott, A. Garcia de La Garza, E. D. Gennatas, M. Quarmley, J. E. Schmitt, R. T. Shinohara, M. D. Tisdall, R. C. Craddock, R. E. Gur, R. C. Gur, T. D. Satterthwaite, Quantitative assessment of structural image quality. *Neuroimage* **169**, 407–418 (2018).
 78. D. R. Roalf, M. Quarmley, M. A. Elliott, T. D. Satterthwaite, S. N. Vandekar, K. Ruparel, E. D. Gennatas, M. E. Calkins, T. M. Moore, R. Hopson, K. Prabhakaran, C. T. Jackson, R. Verma, H. Hakonarson, R. C. Gur, R. E. Gur, The impact of quality assurance assessment on diffusion tensor imaging outcomes in a large-scale population-based cohort. *Neuroimage* **125**, 903–919 (2016).
 79. R. Ciric, A. F. G. Rosen, G. Erus, M. Cieslak, A. Adebimpe, P. A. Cook, D. S. Bassett, C. Davatzikos, D. H. Wolf, T. D. Satterthwaite, Mitigating head motion artifact in functional connectivity MRI. *Nat. Protoc.* **13**, 2801–2826 (2018).
 80. N. J. Tustison, P. A. Cook, A. Klein, G. Song, S. R. Das, J. T. Duda, B. M. Kandel, N. van Strien, J. R. Stone, J. C. Gee, B. B. Avants, Large-scale evaluation of ANTs and FreeSurfer cortical thickness measurements. *Neuroimage* **99**, 166–179 (2014).
 81. B. B. Avants, N. J. Tustison, G. Song, P. A. Cook, A. Klein, J. C. Gee, A reproducible evaluation of ANTs similarity metric performance in brain image registration. *Neuroimage* **54**, 2033–2044 (2011).
 82. N. J. Tustison, B. B. Avants, P. A. Cook, Y. Zheng, A. Egan, P. A. Yushkevich, J. C. Gee, N4ITK: Improved N3 bias correction. *IEEE Trans. Med. Imaging* **29**, 1310–1320 (2010).
 83. B. B. Avants, N. J. Tustison, J. Wu, P. A. Cook, J. C. Gee, An open source multivariate framework for n-tissue segmentation with evaluation on public data. *Neuroinformatics* **9**, 381–400 (2011).
 84. A. Klein, S. S. Ghosh, B. Avants, B. T. T. Yeo, B. Fischl, B. Ardekani, J. C. Gee, J. J. Mann, R. V. Parsey, Evaluation of volume-based and surface-based brain image registration methods. *Neuroimage* **51**, 214–220 (2010).
 85. M. Jenkinson, P. Bannister, M. Brady, S. Smith, Improved optimization for the robust and accurate linear registration and motion correction of brain images. *Neuroimage* **17**, 825–841 (2002).
 86. J. L. R. Andersson, S. N. Sotiropoulos, An integrated approach to correction for off-resonance effects and subject movement in diffusion MR imaging. *Neuroimage* **125**, 1063–1078 (2016).
 87. M. Jenkinson, C. F. Beckmann, T. E. J. Behrens, M. W. Woolrich, S. M. Smith, FSL. *Neuroimage* **62**, 782–790 (2012).
 88. L. Parkes, B. Fulcher, M. Yücel, A. Fornito, An evaluation of the efficacy, reliability, and sensitivity of motion correction strategies for resting-state functional MRI. *Neuroimage* **171**, 415–436 (2018).
 89. S. M. Smith, M. Jenkinson, M. W. Woolrich, C. F. Beckmann, T. E. J. Behrens, H. Johansen-Berg, P. R. Bannister, M. De Luca, I. Drobnjak, D. E. Flitney, R. K. Niazy, J. Saunders, J. Vickers, Y. Zhang, N. De Stefano, J. M. Brady, P. M. Matthews, Advances in functional and structural MR image analysis and implementation as FSL. *Neuroimage* **23**, S208–S219 (2004).
 90. R. W. Cox, AFNI: Software for analysis and visualization of functional magnetic resonance neuroimages. *Comput. Biomed. Res.* **29**, 162–173 (1996).
 91. R. Ciric, D. H. Wolf, J. D. Power, D. R. Roalf, G. L. Baum, K. Ruparel, R. T. Shinohara, M. A. Elliott, S. B. Eickhoff, C. Davatzikos, R. C. Gur, R. E. Gur, D. S. Bassett, T. D. Satterthwaite, Benchmarking of participant-level confound regression strategies for the control of motion artifact in studies of functional connectivity. *Neuroimage* **154**, 174–187 (2017).
 92. M. N. Hallquist, K. Hwang, B. Luna, The nuisance of nuisance regression: Spectral misspecification in a common approach to resting-state fMRI preprocessing reintroduces noise and obscures functional connectivity. *Neuroimage* **82**, 208–225 (2013).
 93. F.-C. Yeh, T. D. Verstynen, Y. Wang, J. C. Fernández-Miranda, W.-Y. I. Tseng, Deterministic diffusion fiber tracking improved by quantitative anisotropy. *PLOS ONE* **8**, e80713 (2013).

94. A. Schaefer, R. Kong, E. M. Gordon, T. O. Laumann, X.-N. Zuo, A. J. Holmes, S. B. Eickhoff, B. T. T. Yeo, Local-global parcellation of the human cerebral cortex from intrinsic functional connectivity MRI. *Cereb. Cortex* **28**, 3095–3114 (2018).
95. M. F. Glasser, T. S. Coalson, E. C. Robinson, C. D. Hacker, J. Harwell, E. Yacoub, K. Ugurbil, J. Andersson, C. F. Beckmann, M. Jenkinson, S. M. Smith, D. C. Van Essen, A multi-modal parcellation of human cerebral cortex. *Nature* **536**, 171–178 (2016).
96. M. A. de Reus, M. P. van den Heuvel, Estimating false positives and negatives in brain networks. *Neuroimage* **70**, 402–409 (2013).
97. R. Vos de Wael, O. Benkarim, C. Paquola, S. Larivière, J. Royer, S. Tavakol, T. Xu, S.-J. Hong, G. Langs, S. Valk, B. Misis, M. Milham, D. Margulies, J. Smallwood, B. C. Bernhardt, BrainSpace: A toolbox for the analysis of macroscale gradients in neuroimaging and connectomics datasets. *Commun Biol.* **3**, 103 (2020).
98. F. Pedregosa, G. Varoquaux, A. Gramfort, V. Michel, B. Thirion, O. Grisel, M. Blondel, P. Prettenhofer, R. Weiss, V. Dubourg, J. Vanderplas, A. Passos, D. Cournapeau, M. Brucher, M. Perrot, É. Duchesnay, Scikit-learn: Machine learning in Python. *J. Mach. Learn. Res.* **12**, 2826–2830 (2011).
99. G. Varoquaux, P. R. Raamana, D. A. Engemann, A. Hoyos-Idrobo, Y. Schwartz, B. Thirion, Assessing and tuning brain decoders: Cross-validation, caveats, and guidelines. *Neuroimage* **145**, 166–179 (2017).
100. S. M. Mitchell, S. Lange, H. Brus, Gendered citation patterns in international relations journals. *Int. Stud. Perspect.* **14**, 485–492 (2013).
101. M. L. Dion, J. L. Sumner, S. M. Mitchell, Gendered citation patterns across political science and social science methodology fields. *Polit. Anal.* **26**, 312–327 (2018).
102. N. Caplar, S. Tacchella, S. Birrer, Quantitative evaluation of gender bias in astronomical publications from citation counts. *Nat. Astron.* **1**, 0141 (2017).
103. D. Maliniak, R. Powers, B. F. Walter, The gender citation gap in international relations. *Int. Org.* **67**, 889–922 (2013).
104. J. D. Dworkin, K. A. Linn, E. G. Teich, P. Zurn, R. T. Shinohara, D. S. Bassett, The extent and drivers of gender imbalance in neuroscience reference lists. *Nat. Neurosci.* **23**, 918–926 (2020).
105. M. A. Bertolero, J. D. Dworkin, S. U. David, C. L. Lloreda, P. Srivastava, J. Stiso, D. Zhou, K. Dzirasa, D. A. Fair, A. N. Kaczkurkin, B. J. Marlin, D. Shohamy, L. Q. Uddin, P. Zurn, D. S. Bassett, Racial and ethnic imbalance in neuroscience reference lists and intersections with gender. *bioRxiv*, 2020.10.12.336230 (2020).
106. X. Wang, J. D. Dworkin, D. Zhou, J. Stiso, E. B. Falk, D. S. Bassett, P. Zurn, D. M. Lydon-Staley, Gendered citation practices in the field of communication. *Ann. Int. Commun. Assoc.* **45**, 134–153 (2021).
107. P. Chatterjee, R. M. Werner, Gender disparity in citations in high-impact journal articles. *JAMA Netw. Open* **4**, e2114509 (2021).
108. J. M. Fulvio, I. Akinola, B. R. Postle, Gender (Im)balance in citation practices in cognitive neuroscience. *J. Cogn. Neurosci.* **33**, 3–7 (2021).
109. D. Zhou, E. J. Cornblath, J. Stiso, E. G. Teich, J. D. Dworkin, A. S. Blevins, D. S. Bassett, Gender diversity statement and code notebook v1.0 (2020), doi:10.5281/ZENODO.3672110.
110. A. Ambekar, C. Ward, J. Mohammed, S. Male, S. Skiena, Name-ethnicity classification from open sources, in *Proceedings of the 15th ACM SIGKDD International Conference on Knowledge Discovery and Data Mining - KDD '09* (ACM Press, Paris, France, 2009), p. 49.
111. G. Sood, S. Laohaprapanon, Predicting race and ethnicity from the sequence of characters in a name (2018), doi:10.48550/ARXIV.1805.02109.

Acknowledgments

Funding: This work was supported by the National Institute of Mental Health grants K99MH127296 (L.P.), R21MH106799 (D.S.B. and T.D.S.), R01MH113550 (D.S.B. and T.D.S.), RF1MH116920 (D.S.B. and T.D.S.), R01MH120482 (T.D.S.), R01MH107703 (T.D.S.), R01MH112847 (T.D.S. and R.T.S.), R37MH125829 (T.D.S.), R01EB022573 (T.D.S.), R01MH107235 (R.C.G.), R01MH119219 (R.C.G. and R.E.G.), R01MH119185 (D.R.R.), R01MH120174 (D.R.R.), R01MH113565 (D.H.W.), and RC2MH089983 and RC2MH089924 (Philadelphia Neurodevelopmental Cohort). The content is solely the responsibility of the authors and does not necessarily represent the official views of the NIH. This work was also supported by the following: NARSAD Young Investigator Grant 28995 from the Brain & Behavior Research Foundation (L.P.), Swartz Foundation (D.S.B.), John D. and Catherine T. MacArthur Foundation (D.S.B.), Penn-CHOP Lifespan Brain Institute, and NSF grant DGE-1321851 (J.Z.K.). **Author contributions:** Conceptualization: L.P., D.S.B., and T.D.S. Methodology: L.P., J.Z.K., J.S., R.T.S., and D.S.B. Software: L.P., J.Z.K., J.S., and M.O. Formal analysis: L.P. Visualization: L.P. and M.O. Data curation: M.E.C., M.C., R.E.G., R.C.G., T.M.M., D.R.R., R.T.S., D.H.W., and T.D.S. Writing—original draft: L.P. Writing—reviewing and editing: L.P., J.Z.K., J.S., M.E.C., M.C., R.E.G., R.C.G., T.M.M., M.O., D.R.R., R.T.S., D.H.W., T.D.S., and D.S.B. **Competing interests:** R.T.S. receives consulting compensation from Octave Bioscience and compensation for reviewership duties from the American Medical Association. All other authors declare that they have no competing interests. **Data and materials availability:** All data needed to evaluate the conclusions in the paper are present in the paper and/or the Supplementary Materials. The PNC data are publicly available in the Database of Genotypes and Phenotypes: accession number phs000607.v3.p2 (www.ncbi.nlm.nih.gov/projects/gap/cgi-bin/study.cgi?study_id=phs000607.v3.p2). All analysis code is available at <https://doi.org/10.5281/zenodo.7133119> and https://github.com/lindenmp/nct_hierarchy.

Submitted 27 May 2022

Accepted 10 November 2022

Published 14 December 2022

10.1126/sciadv.add2185

Asymmetric signaling across the hierarchy of cytoarchitecture within the human connectome

Linden Parkes, Jason Z. Kim, Jennifer Stiso, Monica E. Calkins, Matthew Cieslak, Raquel E. Gur, Ruben C. Gur, Tyler M. Moore, Mathieu Ouellet, David R. Roalf, Russell T. Shinohara, Daniel H. Wolf, Theodore D. Satterthwaite, and Dani S. Bassett

Sci. Adv., **8** (50), eadd2185.
DOI: 10.1126/sciadv.add2185

View the article online

<https://www.science.org/doi/10.1126/sciadv.add2185>

Permissions

<https://www.science.org/help/reprints-and-permissions>

Use of this article is subject to the [Terms of service](#)

Science Advances (ISSN) is published by the American Association for the Advancement of Science. 1200 New York Avenue NW, Washington, DC 20005. The title *Science Advances* is a registered trademark of AAAS.

Copyright © 2022 The Authors, some rights reserved; exclusive licensee American Association for the Advancement of Science. No claim to original U.S. Government Works. Distributed under a Creative Commons Attribution NonCommercial License 4.0 (CC BY-NC).